



RESEARCH ARTICLE

10.1002/2017JC012857

Three-Dimensional Sediment Dynamics in Well-Mixed Estuaries: Importance of the Internally Generated Overtide, Spatial Settling Lag, and Gravitational Circulation

Xiaoyan Wei^{1,2} , Mohit Kumar¹, and Henk M. Schuttelaars¹ ¹Applied Mathematics, Delft University of Technology, Delft, the Netherlands, ²Now at National Oceanography Centre, Liverpool, UK

Key Points:

- Transport of M_2 suspended sediment concentrations by M_2 velocities dominates the landward transport in the idealized Delaware estuary
- Coarse sediments are mostly trapped in the channel near the salt intrusion limit while fine sediments mostly trapped on downstream shoals
- The influence of gravitational circulation on sediment transport increases significantly with increasing river discharge

Correspondence to:

X. Wei,
xywei1988@hotmail.com

Citation:

Wei, X., Kumar, M., & Schuttelaars, H. M. (2018). Three-dimensional sediment dynamics in well-mixed estuaries: importance of the internally generated overtide, spatial settling lag, and gravitational circulation. *Journal of Geophysical Research: Oceans*, 123. <https://doi.org/10.1002/2017JC012857>

Received 3 MAR 2017

Accepted 12 DEC 2017

Accepted article online 27 DEC 2017

Abstract To investigate the dominant sediment transport and trapping mechanisms, a semi-analytical three-dimensional model is developed resolving the dynamic effects of salt intrusion on sediment in well-mixed estuaries in morphodynamic equilibrium. As a study case, a schematized estuary with a converging width and a channel-shoal structure representative for the Delaware estuary is considered. When neglecting Coriolis effects, sediment downstream of the estuarine turbidity maximum (ETM) is imported into the estuary through the deeper channel and exported over the shoals. Within the ETM region, sediment is transported seaward through the deeper channel and transported landward over the shoals. The largest contribution to the cross-sectionally integrated seaward residual sediment transport is attributed to the advection of tidally averaged sediment concentrations by river-induced flow and tidal return flow. This contribution is mainly balanced by the residual landward sediment transport due to temporal correlations between the suspended sediment concentrations and velocities at the M_2 tidal frequency. The M_2 sediment concentration mainly results from spatial settling lag effects and asymmetric bed shear stresses due to interactions of M_2 bottom velocities and the internally generated M_4 tidal velocities, as well as the salinity-induced residual currents. Residual advection of tidally averaged sediment concentrations also plays an important role in the landward sediment transport. Including Coriolis effects hardly changes the cross-sectionally integrated sediment balance, but results in a landward (seaward) sediment transport on the right (left) side of the estuary looking seaward, consistent with observations from literature. The sediment transport/trapping mechanisms change significantly when varying the settling velocity and river discharge.

1. Introduction

An estuarine turbidity maximum (ETM) is a region where the suspended sediment concentration is elevated compared to concentrations upstream or downstream of that region. Estuarine turbidity maxima can have strong implications for estuarine morphology, ecology and biology, because of a continuous deposition of particulate matter that often contains contaminants (de Jonge et al., 2014; Jay & Musiak, 1994; Jay et al., 2015; Lin & Kuo, 2003; Sanford et al., 2001; Schoellhamer et al., 2007). Furthermore, these high turbidity levels result in reduced light availability and oxygen levels (de Jonge et al., 2014; McSweeney et al., 2016a; Talke et al., 2009). ETM's are often located at regions of low salinities (Grabemann et al., 1997), but they can also be found in regions with larger salinities (Gibbs et al., 1983; Lin & Kuo, 2001) or even at fixed locations independent of salinity (Jay & Musiak, 1994; Lin & Kuo, 2001). This large variability in sediment trapping locations highlights the importance to identify the dominant mechanisms resulting in the ETM formation.

Process-based models have been intensively used to investigate sediment transport and trapping. Complex process-based models (see e.g., Ralston et al., 2012; Van Maren et al., 2015) are often used to investigate a specific estuary in detail. These models take into account observed estuarine bathymetry, geometry and forcing conditions and include all known physical processes and state-of-the-art parameterizations, thus allowing for a quantitative comparison of the model results with observations. Due to their complexity, these models are often solved numerically, which complicates the assessment of the influence of physical mechanisms in isolation. Furthermore, due to their long run-time, these models are not commonly used for systematic sensitivity studies.

© 2017. The Authors.

This is an open access article under the terms of the Creative Commons Attribution-NonCommercial-NoDerivs License, which permits use and distribution in any medium, provided the original work is properly cited, the use is non-commercial and no modifications or adaptations are made.

Idealized process-based models, which focus on specific processes using idealized geometries and bathymetries, are effective tools to systematically investigate the dominant trapping mechanisms and study the sensitivity of these mechanisms to model parameters. Idealized models have been developed to investigate the cross-sectionally averaged (1-D) processes (Friedrichs et al., 1998; De Swart & Zimmerman, 2009; Winterwerp, 2011), width-averaged (longitudinal-vertical, 2DV) processes (Burchard & Baumert, 1998; Chernetsky et al., 2010; de Jonge et al., 2014; Geyer, 1993; Jay & Musiak, 1994; Schuttelaars et al., 2013; Talke et al., 2009), or lateral processes assuming along-channel uniform conditions (Huijts et al., 2006, 2011; Yang et al., 2014). The results of the width-averaged models show that the formation and maintenance of the ETM can often be attributed to the convergence of residual seaward sediment transport upstream of the ETM induced by river discharge, and residual landward sediment transport downstream of the ETM resulting from various mechanisms. These mechanisms include the salinity-induced gravitational circulation (Festa & Hansen, 1978; Postma, 1967), settling lag effects and tidal asymmetry (Chernetsky et al., 2010; De Swart & Zimmerman, 2009; Friedrichs et al., 1998; Lin & Kuo, 2001; Winterwerp & Wang, 2013), tidal straining (Burchard & Baumert, 1998; Burchard et al., 2004; Scully & Friedrichs, 2007), stratification induced by salinity (Geyer, 1993) or sediment concentration (Winterwerp, 2011), sediment-induced currents (Talke et al., 2009), flocculation and hindered settling (Winterwerp, 2011). Focusing on the lateral sediment trapping mechanisms, Huijts et al. (2006, 2011) showed that the lateral density gradient was crucial for the lateral sediment trapping, while trapping due to the Coriolis effects was less important. Extending the work of Huijts et al. (2006, 2011), Yang et al. (2014) found that the effects of the lateral density gradient, M_4 tidal flow and spatial settling lag all played an important role in the lateral sediment trapping. The above-mentioned references clearly show that most idealized models either focus on longitudinal or lateral processes, even though observational studies have shown that both lateral and longitudinal processes, and especially their interaction, can be important to the along-channel and cross-channel sediment transport and trapping in estuaries (Becherer et al., 2016; Fugate et al., 2007; McSweeney et al., 2016b; Sommerfield & Wong, 2011). To investigate the importance of the three-dimensional (3-D) sediment trapping mechanisms, Kumar et al. (2017) developed a semi-analytical three-dimensional model combining the longitudinal and lateral approaches of Chernetsky et al. (2010) and Huijts et al. (2006) in a consistent way. However, the resulting model is still diagnostic in salinity, thus the dynamic effects of salinity-induced gravitational circulation on sediment transport and trapping, which are potentially important, are not included.

The aim of this paper is to develop a three-dimensional semi-analytical model that allows for a systematical analysis of the sediment trapping and transport mechanisms, explicitly resolving the dynamic effects of salinity. Flocculation effects are ignored by considering only noncohesive sediments. First, the coupled water motion and salinity are obtained. Using this information, the sediment transport and distribution are calculated. This approach allows for a systematical analysis of the three-dimensional sediment trapping mechanisms and the importance of each individual mechanism for the ETM formation. In this paper, a schematized estuary is considered, with characteristics representative for the Delaware estuary, in which both lateral and longitudinal circulations are significant (McSweeney et al., 2016a, 2016b). Moreover, since the location of sediment trapping can change significantly with varying settling velocity and river discharge (Aubrey, 1986; de Jonge et al., 2014; Jay et al., 2015; Uncles & Stephens, 1993), a sensitivity study of the three-dimensional sediment trapping locations and mechanisms for these two factors is conducted.

The structure of this paper is as follows: in section 2, the idealized model is introduced, including the governing equations and corresponding boundary conditions (section 2.1), a brief introduction of the adopted semi-analytical method (section 2.2) and an analytical decomposition of the sediment transport mechanisms (section 2.3). In section 3, the default experiment using parameters representative for the Delaware estuary, but neglecting Coriolis effects, is studied to show the 3-D sediment trapping mechanisms. The influence of Coriolis deflection is investigated in section 4. Next, a sensitivity study of the sediment trapping mechanisms for the sediment settling velocity and river discharge is presented in section 5. The above-mentioned sensitivity and the limitations of the present idealized model are discussed in section 6. Some conclusions are drawn in section 7.

2. Model Description

The semi-analytical idealized three-dimensional (3-D) model presented in this paper consists of the shallow water equations, dynamically coupled to the salinity module described in Wei et al. (2017) and to the

sediment module of Kumar et al. (2017). The estuary is assumed to be well-mixed and tidally dominated. Since the coupled water motion and salinity are calculated simultaneously, the salinity effects on the water motion and sediment transport are dynamically obtained.

In section 2.1, the systems of equations governing the water motion, salinity and sediment dynamics, together with the corresponding boundary conditions are introduced; the solution method is briefly introduced in section 2.2; the analytical decomposition of the sediment transport mechanisms is introduced in section 2.3.

2.1. Governing Equations and Boundary Conditions

The estuary under consideration is forced by tides at the seaward boundary ($\partial_S\Omega$) and a river discharge at the landward boundary ($\partial_R\Omega$), where a weir is located (see Figure 1). The closed boundaries ($\partial_C\Omega$) are impermeable. The undisturbed water level is located at $z = 0$, and the free surface elevation is denoted by $z = \eta$. The estuarine bathymetry varies in the horizontal directions $z = -H(x, y)$, with H an arbitrary function of the horizontal coordinates (x, y) .

The water motion is governed by the 3-D shallow water equations assuming hydrostatic equilibrium and using the Boussinesq approximation:

$$\frac{\partial u}{\partial x} + \frac{\partial v}{\partial y} + \frac{\partial w}{\partial z} = 0, \quad (1)$$

$$\frac{\partial u}{\partial t} + \nabla \cdot (\mathbf{U}u) - fv = -g \frac{\partial \eta}{\partial x} - \frac{g}{\rho_c} \int_z^{\eta} \frac{\partial \rho}{\partial x} dz + \frac{\partial}{\partial z} \left(A_v \frac{\partial u}{\partial z} \right), \quad (2)$$

$$\frac{\partial v}{\partial t} + \nabla \cdot (\mathbf{U}v) + fu = -g \frac{\partial \eta}{\partial y} - \frac{g}{\rho_c} \int_z^{\eta} \frac{\partial \rho}{\partial y} dz + \frac{\partial}{\partial z} \left(A_v \frac{\partial v}{\partial z} \right). \quad (3)$$

Here t denotes time, $\mathbf{U} = (u, v, w)$ is the velocity vector, with u, v and w the velocity components in x, y and z directions, respectively. The acceleration of gravity is denoted by g , with a value of $9.8 \text{ m}^2 \cdot \text{s}^{-1}$. A_v is the vertical eddy viscosity coefficient. Following Winant (2008) and Kumar et al. (2017), the horizontal viscous effects are neglected. The Coriolis parameter is denoted by f . The estuarine water density ρ is assumed to depend only on the salinity S as $\rho = \rho_c(1 + \beta_s S)$, with $\beta_s = 7.6 \times 10^{-4} \text{ psu}^{-1}$ and ρ_c the background density, taken to be $1,000 \text{ kg} \cdot \text{m}^{-3}$. To dynamically calculate the density, the salinity equation needs to be solved:

$$\frac{\partial S}{\partial t} + \nabla \cdot (\mathbf{U}S) = \frac{\partial}{\partial x} \left(K_h \frac{\partial S}{\partial x} \right) + \frac{\partial}{\partial y} \left(K_h \frac{\partial S}{\partial y} \right) + \frac{\partial}{\partial z} \left(K_v \frac{\partial S}{\partial z} \right), \quad (4)$$

with K_h and K_v (assumed to be equal to A_v) the horizontal and vertical diffusivity coefficients, respectively. The suspended sediment concentration (SSC) equation reads

$$\frac{\partial C}{\partial t} + \nabla \cdot (\mathbf{U}C) - \frac{\partial (w_s C)}{\partial z} = \frac{\partial}{\partial x} \left(K_h \frac{\partial C}{\partial x} \right) + \frac{\partial}{\partial y} \left(K_h \frac{\partial C}{\partial y} \right) + \frac{\partial}{\partial z} \left(K_v \frac{\partial C}{\partial z} \right), \quad (5)$$

where w_s is the sediment settling velocity and strongly depends on the sediment grain size (Fredsoe & Deigaard, 1992).

At the closed boundaries, $\partial_C\Omega$, the normal depth-integrated water flux and the tidally averaged salt and sediment transports are required to vanish. At the river boundary $\partial_R\Omega$, a river discharge Q is prescribed, while the normal tidally averaged salt and sediment transports have to vanish, for details see Wei et al. (2017) and Kumar et al. (2017). At the seaward boundaries, the water motion is forced by a prescribed

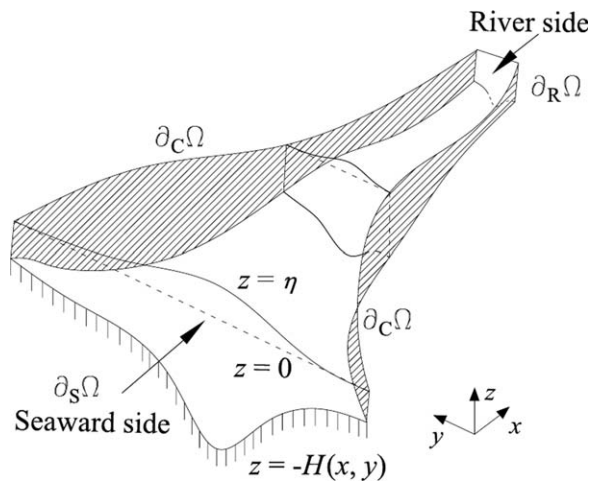


Figure 1. A three-dimensional sketch of the estuary, with x and y the horizontal coordinates, and z the vertical coordinate, positive in the upward direction. The seaward, river, and closed boundaries are denoted by $\partial_S\Omega$, $\partial_R\Omega$, and $\partial_C\Omega$, respectively. The free surface elevation and the estuarine bottom are located at $z = \eta$ and $z = -H(x, y)$, respectively. This sketch is taken from Wei et al. (2017).

sea surface elevation that consists of a semi-diurnal tidal constituent (M_2), its first overtide (M_4), and a residual sea surface elevation (M_0):

$$\eta(x, y, t) = a_{M_2}(x, y) \cos[\sigma_{M_2} t - \varphi_{M_2}(x, y)] + a_{M_4}(x, y) \cos[2\sigma_{M_2} t - \varphi_{M_4}(x, y)] + a_{M_0}(x, y) \quad \text{at } (x, y) \in \partial_S \Omega, \quad (6)$$

where a_{M_2} , a_{M_4} , φ_{M_2} and φ_{M_4} are the prescribed amplitude and phase of the semi-diurnal and its first overtide at the seaward boundary $\partial_S \Omega$, respectively. Here $\sigma_{M_2} \sim 1.4 \times 10^{-4} \text{ s}^{-1}$ denotes the M_2 tidal frequency. The prescribed residual sea surface elevation at $\partial_S \Omega$ is denoted by $a_{M_0}(x, y)$. The tidally averaged salinity and suspended sediment concentration are prescribed at $\partial_S \Omega$,

$$\bar{S} = S_e(x, y), \quad \bar{C} = C_m(x, y) \quad \text{at } (x, y) \in \partial_S \Omega, \quad (7)$$

with the overbar $\bar{\cdot}$ denoting a tidal average. Note that the seaward boundary condition for the sediment concentration in (7) is different from that used in Kumar et al. (2017), where the normal (depth-integrated) sediment transport is required to vanish at each location of the seaward boundary. Using boundary condition (7) allows a pointwise nonzero sediment transport over the seaward boundary. In equilibrium, the cross-sectionally integrated sediment transport has to vanish due to the no-transport condition at the closed and river boundaries.

For the water motion, the kinematic and no stress boundary conditions are prescribed at the free surface ($z = \eta$):

$$w = \frac{\partial \eta}{\partial t} + u \frac{\partial \eta}{\partial x} + v \frac{\partial \eta}{\partial y}, \quad (8)$$

$$A_v \frac{\partial u}{\partial z} = A_v \frac{\partial v}{\partial z} = 0. \quad (9)$$

At the bottom ($z = -H$), the normal velocity is required to vanish and a partial slip condition is applied (Schramkowski & De Swart, 2002):

$$w = -\frac{\partial H}{\partial x} u - \frac{\partial H}{\partial y} v, \quad (10)$$

$$A_v \left(\frac{\partial u}{\partial z}, \frac{\partial v}{\partial z} \right) = \frac{\tau_b^h}{\rho_c} = s(u, v). \quad (11)$$

The slip parameter s depends on the bed roughness and follows from linearizing the horizontal component of the bed shear stress τ_b^h . Here the horizontal bed shear stress is used because the depth gradients are assumed to be small, thus the vertical component of the bed shear stress is negligible. Concerning the salinity dynamics, the salt flux is required to vanish at the free surface and the bottom.

The normal sediment flux is required to vanish at the surface,

$$\left(K_h \frac{\partial C}{\partial x}, K_h \frac{\partial C}{\partial y}, K_v \frac{\partial C}{\partial z} + w_s C \right) \cdot \vec{n}_\eta = 0 \quad \text{at } z = \eta, \quad (12)$$

with \vec{n}_η the normal vector at the free surface, pointing upward: $\vec{n}_\eta = \left(-\frac{\partial \eta}{\partial x}, -\frac{\partial \eta}{\partial y}, 1 \right)$. The normal component of the diffusive sediment flux at the bottom is related to the erosion flux $E = w_s C_{\text{ref}}$ by

$$\left(K_h \frac{\partial C}{\partial x}, K_h \frac{\partial C}{\partial y}, K_v \frac{\partial C}{\partial z} \right) \cdot \vec{n}_b = w_s C_{\text{ref}} \quad \text{at } z = -H(x, y), \quad (13)$$

with $\vec{n}_b = \left(-\frac{\partial H}{\partial x}, -\frac{\partial H}{\partial y}, -1 \right)$ the normal vector at the bottom pointing downward. The reference concentration is denoted by C_{ref} , and is proportional to the bed shear stress and the sediment availability a :

$$C_{\text{ref}} = \frac{\rho_s a |v_b^h|}{\rho_0 g' d_s}. \quad (14)$$

Here ρ_s denotes the sediment density, $g' = g(\rho_s - \rho_0) / \rho_0$ the reduced gravity and d_s the sediment grain size. The mean water density ρ_0 takes into account the effects of salt on water density and is assumed to be a constant. The sediment availability a is an erosion coefficient that accounts for the amount of easily erodible sediment available in a mud reach (Chernetsky et al., 2010; Friedrichs et al., 1998; Huijts et al., 2006).

At this point, the sediment availability a is still unknown. By assuming the estuary to be in morphodynamic equilibrium (the tidally averaged sediment deposition and erosion balance each other, for details, see Friedrichs et al., 1998; Kumar et al., 2017), the spatial distribution of a follows from solving the tidally averaged and depth-integrated sediment equation

$$\frac{\partial}{\partial x} \int_{-H}^{\eta} \left(Cu - K_h \frac{\partial C}{\partial x} \right) dz + \frac{\partial}{\partial y} \int_{-H}^{\eta} \left(Cv - K_h \frac{\partial C}{\partial y} \right) dz = 0, \quad (15)$$

using boundary conditions (7), (12), (13), and no normal sediment transport conditions at the closed and landward boundaries.

2.2. Solution Method

To identify the relative importance of different mechanisms governing the sediment dynamics, a semi-analytical approach is used to solve equations (1)–(15). In this approach, we employ a perturbation method to get an ordered system of equations which are partly solved analytically and partly numerically using a finite element method. The perturbation method is originally developed by Ianniello (1977) to derive analytic solutions for the width-averaged tidally induced residual currents, which was later used in McCarthy (1993) to calculate the width-averaged density-induced residual currents in well-mixed estuaries. As a first step of the perturbation method, all physical variables are scaled by their typical values, resulting in a nondimensional system of equations. The dimensionless numbers that indicate the relative importance of the various terms are then compared to the small parameter ε , with ε the ratio between the M_2 tidal amplitude to the water depth averaged over the seaward boundary. Next, terms of the same order in ε are collected, resulting in a system of equations at each order of ε that can be solved separately. The vertical structure of all physical variables describing the water motion, salinity and sediment concentration are obtained analytically, while their horizontal structures have to be calculated numerically. Here we use a finite element method (for details, see Kumar et al., 2016, 2017; Wei et al., 2017) to get the horizontal dependencies. Using this approach, the barotropic water motion, including the residual (M_0) flow, and the M_2 and M_4 tidal flow can be explicitly calculated. However, since the baroclinic residual flow (i.e., gravitational circulation) is dynamically coupled to salinity, an iterative approach is needed to simultaneously calculate the gravitational circulation and the salinity field (for details, see Wei et al., 2017). After calculating the necessary water motion constituents (M_0 , M_2 , M_4), the suspended sediment concentration at each order of ε can be expressed in terms of the sediment availability, which follows from the morphodynamic equilibrium condition (Kumar et al., 2017).

2.3. An Analytical Decomposition

Using the solution method sketched above and neglecting terms of $O(\varepsilon^2)$ and higher, the flow velocity can be analytically decomposed into two tidal constituents and a residual component:

$$\mathbf{U} = \underbrace{\mathbf{U}_{M_2}}_{O(1)} + \underbrace{\mathbf{U}_{M_4} + \mathbf{U}_{M_0}}_{O(\varepsilon)}. \quad (16)$$

Here \mathbf{U}_{M_2} is the leading-order tidal velocity vector at the M_2 tidal frequency (at $O(1)$), \mathbf{U}_{M_4} is the first-order tidal velocity vector at the M_4 tidal frequency (at $O(\varepsilon)$), and \mathbf{U}_{M_0} is the $O(\varepsilon)$ subtidal flow velocity vector. The M_2 component of the flow velocity \mathbf{U}_{M_2} is externally forced by a prescribed M_2 tide at the entrance. Its first overtide \mathbf{U}_{M_4} consists of various contributions:

$$\mathbf{U}_{M_4} = \mathbf{U}_{M_4}^{\text{EF}} + \mathbf{U}_{M_4}^{\text{AC}} + \mathbf{U}_{M_4}^{\text{NS}} + \mathbf{U}_{M_4}^{\text{TRF}}. \quad (17)$$

The first contribution $\mathbf{U}_{M_4}^{\text{EF}}$ results from an external M_4 forcing prescribed at the mouth, while other contributions are generated internally by nonlinear interactions of the M_2 tidal constituent: tidal rectification ($\mathbf{U}_{M_4}^{\text{AC}}$), the stress-free condition ($\mathbf{U}_{M_4}^{\text{NS}}$, as the shear stress is required to vanish at $z=\eta$ instead of $z=0$) and tidal return flow ($\mathbf{U}_{M_4}^{\text{TRF}}$). In this paper, tidal return flow ($\mathbf{U}_{M_4}^{\text{TRF}}$, $\mathbf{U}_{M_0}^{\text{TRF}}$) refers to the water flow associated with the Stokes' drift and the return flow compensating the M_4/M_0 component of the Stokes' drift contribution. A more detailed explanation and formulation for different flow components can be found in section 5 of Kumar et al. (2017). The residual flow \mathbf{U}_{M_0} is analytically decomposed into different components as well:

$$\mathbf{U}_{M_0} = \mathbf{U}_{M_0}^{\text{RD}} + \mathbf{U}_{M_0}^{\text{GC}} + \mathbf{U}_{M_0}^{\text{AC}} + \mathbf{U}_{M_0}^{\text{NS}} + \mathbf{U}_{M_0}^{\text{TRF}}. \quad (18)$$

Here $\mathbf{U}_{M_0}^{\text{RD}}$ results from the externally prescribed river discharge. Other contributions are related to the salinity-induced gravitational circulation ($\mathbf{U}_{M_0}^{\text{GC}}$), the nonlinear interactions due to tidal rectification ($\mathbf{U}_{M_0}^{\text{AC}}$), the stress-free surface condition ($\mathbf{U}_{M_0}^{\text{NS}}$) and tidal return flow ($\mathbf{U}_{M_0}^{\text{TRF}}$). In the asymptotic expansion, both \mathbf{U}_{M_4} and \mathbf{U}_{M_0} are of $O(\varepsilon)$.

Substituting equation (16) into (11) and making a Taylor expansion with respect to the small parameter ε , it follows that $|\tau_b^h|$ can be decomposed into Fourier series consisting of a residual component and all frequencies that are a multiple of the M_2 tidal frequency,

$$|\tau_b^h| = \rho s \sqrt{u^2 + v^2} = \underbrace{\left(|\tau_{b_{M_0}}| + |\tau_{b_{M_4}}| + |\tau_{b_{M_8}}| + \dots \right)}_{O(1)} + \underbrace{\left(|\tau_{b_{M_2}}| + |\tau_{b_{M_6}}| + \dots \right)}_{O(\varepsilon)} + \dots \quad (19)$$

Equation (19) shows that, when ignoring the difference in the amplitudes of different Fourier components, the residual bed shear stress $\tau_{b_{M_0}}$, and all bed shear stresses of frequencies which are even multiples of the M_2 tidal frequency ($\tau_{b_{M_4}}$, $\tau_{b_{M_8}}$, ...) resulting from the M_2 bottom velocity, are leading-order contributions. The other components ($\tau_{b_{M_2}}$, $\tau_{b_{M_6}}$, ...) result from the interactions of the M_2 bottom velocity with the residual and M_4 bottom velocities, and are of $O(\varepsilon)$. From equations (13), (14), and (19), it follows that the resulting suspended sediment concentration is given by

$$\mathbf{C} = \underbrace{\left(\mathbf{C}_{M_0} + \mathbf{C}_{M_4} + \mathbf{C}_{M_8} + \dots \right)}_{O(1)} + \underbrace{\left(\mathbf{C}_{M_2} + \mathbf{C}_{M_6} + \dots \right)}_{O(\varepsilon)} + \dots, \quad (20)$$

i.e., it consists of contributions at different tidal frequencies. It can be shown that C_{M_0} , C_{M_4} (and C_{M_8}, \dots) are leading-order concentrations, and C_{M_2} (and C_{M_6}, \dots) are first-order concentrations. However, equations (19) and (20) do not mean the M_8 (and higher) frequencies of the bed shear stress and SSC have to be as significant as the components at M_0 and M_4 frequencies, because the amplitudes of M_0 and M_4 components in the Fourier series are much larger than those of M_8 and higher frequencies. The leading-order concentrations are induced by the bed shear stress due to M_2 bottom velocity. The first-order concentrations, however, are caused both by the asymmetric bed shear due to the combined M_2 and M_0/M_4 bottom velocities, and by the advection of the leading-order concentrations by the M_2 tidal velocity (\mathbf{U}_{M_2}). Moreover, the vanishing normal sediment flux prescribed at the free surface introduces a first-order sediment flux at $z=0$, which also results in a first-order contribution in the sediment concentrations C_{M_2} (Kumar et al., 2017).

It is important to note that to obtain the dominant sediment transport balance, only the leading-order concentrations C_{M_0} and C_{M_4} , and the first-order concentration C_{M_2} are needed. Using this information, substituting equations (16), (18), (20) into (15), the depth-integrated, tidally averaged sediment transport equation becomes

$$\begin{aligned}
 & \nabla \cdot \left(\underbrace{\int_{-H}^0 u_{M_0} C_{M_0} dz + \overline{\eta_{M_2} u_{M_2}}|_{z=0} C_{M_0}|_{z=0}}_{\mathbf{T}_{M_0}} \right) + \nabla \cdot \left(\underbrace{\int_{-H}^0 \overline{u_{M_2} C_{M_2}} dz}_{\mathbf{T}_{M_2}} \right) \\
 & + \nabla \cdot \left(\underbrace{\int_{-H}^0 \overline{v_{M_0} C_{M_0}} dz + \overline{\eta_{M_2} v_{M_2}}|_{z=0} C_{M_0}|_{z=0}}_{\mathbf{T}_{M_0}} \right) + \nabla \cdot \left(\underbrace{\int_{-H}^0 \overline{v_{M_2} C_{M_2}} dz}_{\mathbf{T}_{M_2}} \right) \\
 & + \nabla \cdot \left(\underbrace{\int_{-H}^0 \overline{u_{M_4} C_{M_4}} dz + \overline{\eta_{M_2} u_{M_2}}|_{z=0} C_{M_4}|_{z=0}}_{\mathbf{T}_{M_4}} \right) + \nabla \cdot \left(\underbrace{\int_{-H}^0 \overline{v_{M_4} C_{M_4}} dz + \overline{\eta_{M_2} v_{M_2}}|_{z=0} C_{M_4}|_{z=0}}_{\mathbf{T}_{M_4}} \right) \\
 & + \nabla \cdot \left(\underbrace{-\int_{-H}^0 K_h \frac{\partial C_{M_0}}{\partial x} dz}_{\mathbf{T}_{\text{DIFF}}} \right) + \nabla \cdot \left(\underbrace{-\int_{-H}^0 K_h \frac{\partial C_{M_0}}{\partial y} dz}_{\mathbf{T}_{\text{DIFF}}} \right) = 0.
 \end{aligned} \tag{21}$$

In equation (21), \mathbf{T}_{M_0} , \mathbf{T}_{M_2} and \mathbf{T}_{M_4} represent the depth-integrated residual sediment transport contributions due to different advective transport processes, and \mathbf{T}_{DIFF} denotes transport due to diffusive processes. Here, \mathbf{T}_{M_2} is the depth-integrated residual sediment transport due to the advection of the M_2 tidal concentration C_{M_2} by M_2 tidal velocities. The depth-integrated residual sediment transports due to the advection of the residual concentration C_{M_0} by the residual velocities, and the advection of the M_4 tidal concentration C_{M_4} by the M_4 tidal velocities, are included in \mathbf{T}_{M_0} and \mathbf{T}_{M_4} , respectively.

Following equations (17)–(20), the depth-integrated sediment transport contributions can be further decomposed into different mechanisms as listed in Table 1 (see a more detailed decomposition in Kumar et al., 2017). The sediment transport \mathbf{T}_{M_0} includes transport contributions due to the advection of the residual concentration C_{M_0} by the gravitational circulation ($\mathbf{T}_{M_0}^{\text{GC}}$), and the other barotropic residual flow components ($\mathbf{T}_{M_0}^{\text{BR}}$) as a result of the river-induced flow ($\mathbf{T}_{M_0}^{\text{RD}}$), tidal rectification ($\mathbf{T}_{M_0}^{\text{AC}}$), the stress-free surface boundary condition ($\mathbf{T}_{M_0}^{\text{NS}}$), and tidal return flow ($\mathbf{T}_{M_0}^{\text{TRF}}$). The depth-integrated transport \mathbf{T}_{M_2} includes the M_2 tidal advection of SSC at the M_2 tidal frequency, which is partly a result of the asymmetric bed shear stress due to the interaction of the M_2 tidal velocity and the salinity-induced baroclinic residual current ($\mathbf{T}_{M_2}^{\text{GC}}$) and the internally generated barotropic residual current ($\mathbf{T}_{M_2}^{\text{BR}}$) at the bottom. Moreover, the asymmetric bed shear stress due to interactions of the M_2 bottom velocity and the externally forced ($\mathbf{T}_{M_2}^{\text{EF}}$) or internally generated ($\mathbf{T}_{M_2}^{\text{IN}}$) M_4 tidal currents at the bottom also induce an M_2 tidal concentration, which temporally correlates with the M_2 tidal velocity, and results in a residual sediment transport. Besides, the first-order correction of the leading-order vertical sediment fluxes at the free-surface boundary results in a first-order SSC at the M_2 tidal frequency and thence a sediment transport ($\mathbf{T}_{M_2}^{\text{SC}}$), which is called the surface contribution (Kumar et al., 2017). Finally, the advection of the residual and M_4 tidal components of SSC by the M_2 tidal currents also results in a SSC at the M_2 tidal frequency. Advection of this concentration component by the M_2 tidal currents again results in a residual sediment transport, and is denoted as the spatial settling lag contribution ($\mathbf{T}_{M_2}^{\text{SSL}}$). The transport contribution \mathbf{T}_{M_4} is caused by advection of SSC at the M_4 tidal frequency by the M_4 tidal flow as a result of both the M_4 tidal flow generated internally ($\mathbf{T}_{M_4}^{\text{IN}}$) and the externally forced M_4 tide ($\mathbf{T}_{M_4}^{\text{EF}}$). Owing to the semi-analytical solution method and the analytic approach of decomposition, all decomposed mechanisms listed above can be calculated individually.

Integrating equation (21) from the left bank of the channel ($y=y_1$) to the right bank ($y=y_2$), and subsequently integrating from the weir (at $x=L$) to any longitudinal location x , the cross-sectionally integrated longitudinal residual sediment balance is found:

$$\begin{aligned}
 & \int_{y_1}^{y_2} \left(\underbrace{\int_{-H}^0 u_{M_0} C_{M_0} dz + \overline{\eta_{M_2} u_{M_2}}|_{z=0} C_{M_0}|_{z=0}}_{\mathbf{T}_{M_0}} \right) dy + \int_{y_1}^{y_2} \int_{-H}^0 \overline{u_{M_2} C_{M_2}} dz dy \\
 & + \int_{y_1}^{y_2} \left(\underbrace{\int_{-H}^0 \overline{v_{M_0} C_{M_0}} dz + \overline{\eta_{M_2} v_{M_2}}|_{z=0} C_{M_0}|_{z=0}}_{\mathbf{T}_{M_0}} \right) dy + \int_{y_1}^{y_2} \int_{-H}^0 \overline{v_{M_2} C_{M_2}} dz dy \\
 & + \int_{y_1}^{y_2} \left(\underbrace{\int_{-H}^0 \overline{u_{M_4} C_{M_4}} dz + \overline{\eta_{M_2} u_{M_2}}|_{z=0} C_{M_4}|_{z=0}}_{\mathbf{T}_{M_4}} \right) dy + \int_{y_1}^{y_2} \int_{-H}^0 \overline{v_{M_4} C_{M_4}} dz dy \\
 & + \int_{y_1}^{y_2} \int_{-H}^0 -K_h \frac{\partial C_{M_0}}{\partial x} dz dy + \int_{y_1}^{y_2} \int_{-H}^0 -K_h \frac{\partial C_{M_0}}{\partial y} dz dy = 0.
 \end{aligned} \tag{22}$$

Table 1
Decomposition of the Depth-Integrated Sediment Transports Due to Different Contributions^a

Transport	Decomposition	Concentration	Velocity
T_{M_0}	$T_{M_0}^{GC}$	C_{M_0}	$U_{M_0}^{GC}$
	$T_{M_0}^{RD}$		$U_{M_0}^{RD}$
	$T_{M_0}^{AC}$		$U_{M_0}^{AC}$
	$T_{M_0}^{TRF}$		$U_{M_0}^{TRF}$
	$T_{M_0}^{NS}$		$U_{M_0}^{NS}$
T_{M_2}	$T_{M_2}^{GC}$	C_{M_2} due to $U_{M_2} + U_{M_0}^{GC}$	U_{M_2}
	$T_{M_2}^{BR}$	C_{M_2} due to $U_{M_2} + U_{M_0}^{RD} + U_{M_0}^{AC} + U_{M_0}^{NS} + U_{M_0}^{TRF}$	
	$T_{M_2}^{EF}$	C_{M_2} due to $U_{M_2} + U_{M_4}^{EF}$	
	$T_{M_2}^{IN}$	C_{M_2} due to $U_{M_2} + U_{M_4}^{AC} + U_{M_4}^{NS} + U_{M_4}^{TRF}$	
	$T_{M_2}^{SC}$	C_{M_2} due to surface contribution	
	$T_{M_2}^{SSL}$	C_{M_2} due to spatial settling lag	
T_{M_4}	$T_{M_4}^{IN}$	C_{M_4}	$U_{M_4}^{AC} + U_{M_4}^{NS} + U_{M_4}^{TRF}$
	$T_{M_4}^{EF}$		$U_{M_4}^{EF}$

^aThe same decomposition can be made for the cross-sectionally integrated transport contributions (not shown).

Equation (22) shows that the cross-sectionally integrated along-channel residual sediment balance is maintained by T_{M_0} , T_{M_2} , T_{M_4} , and T_{DIFF} . These transport contributions can be further decomposed in the same way as the depth-integrated sediment transport contribution (not shown).

To analyze all potentially important processes which drive the transport and trapping of SSC in well-mixed estuaries, we will first consider a default experiment with parameter values representative for the Delaware estuary (neglecting Coriolis effects, see section 3). Then, the influence of the Coriolis effects on these processes will be investigated in section 4. After that, the sensitivity of these processes to the sediment settling velocity and river discharge will be analyzed (see section 5).

3. Default Experiment

The estuarine bathymetry, geometry, forcing conditions and parameters for the default experiment are defined in section 3.1. The resulting SSC structures in morphodynamic equilibrium and the depth-integrated sediment transport/trapping patterns are discussed in section 3.2 and 3.3, respectively. To understand the relative importance of various contributions to the along-channel residual sediment transport, the cross-sectionally integrated (along-channel) residual sediment balance is analyzed in section 3.4. The significance of sediment transports associated with the internally generated overtide, spatial settling lag effects and gravitational circulation to the ETM formation is investigated in section 3.5.

3.1. Parameters Setting for the Default Experiment

The default experiment considers a schematized, well-mixed estuary, with an estuarine length (L) of 215 km and a width (B) exponentially converging up-estuary,

$$B = B_0 e^{-x/L_b}. \quad (23)$$

Here $B_0 = 39$ km is the estuarine width at the mouth, and $L_b = 42$ km the estuarine convergence length (representative for the Delaware estuary). Following Wei et al. (2017), the bathymetry exhibits a lateral channel-shoal structure, and is given by

$$H(x, y) = H_{\min} + (H_m - H_{\min}) \frac{x}{L} + (H_{\max} - H_{\min}) \left(1 - \frac{x}{L}\right) \left(1 - \frac{4y^2}{B^2}\right) e^{-C_f \frac{4y^2}{B^2}}, \quad (24)$$

with the maximum water depth $H_{\max} = 15$ m and the minimum water depth $H_{\min} = 3.6$ m on the shoals of the estuarine mouth. The width-averaged water depth $H_m = 8$ m and the tidal flat parameter $C_f = 4$ are constant along the channel.

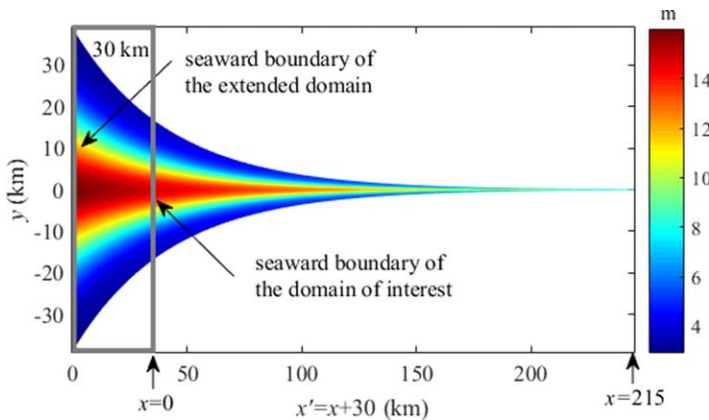


Figure 2. The bathymetry and geometry of the extended domain, and the (nonextended) domain of interest.

In order to obtain a physically consistent solution for the salinity, and to make the sediment distribution at the seaward boundary consistent with that in the interior, the barotropic water motion will be calculated in a domain which is extended 30 km toward the open sea (see gray rectangle in Figure 2). A constant barotropic sea surface elevation is prescribed at the seaward boundary of the extended domain ($x'=0$) such that the width-averaged sea surface elevation η^m at the seaward boundary of the physical domain ($x=0$)

$$\eta^m = a_{M_2}^m \cos(\sigma_{M_2} t) + a_{M_4}^m \cos(2\sigma_{M_2} t - \Delta\varphi^m) + a_{M_0}^m \quad (25)$$

is in agreement with the observations of the Delaware estuary by Walters (1997). Here $a_{M_2}^m$, $a_{M_4}^m$, and $\Delta\varphi^m$ denote the width-averaged M_2 and M_4 tidal amplitudes and the relative phase between the M_2 and M_4 tidal constituents at $x=0$, respectively. $a_{M_0}^m$ is the mean residual water level at $x=0$, and is required to vanish. Following Wei et al. (2017), the residual salinity $x=0$ (S_m) is prescribed to be 31 psu the

horizontal diffusivity K_h is assumed to linearly decrease with B , from $50 \text{ m}^2 \cdot \text{s}^{-1}$ at the mouth to $10 \text{ m}^2 \cdot \text{s}^{-1}$ at the landward side.

After calculating the barotropic water motion in the extended domain, the (baroclinic) gravitational circulation and salinity distribution are calculated for the domain of interest (between $x=0$ and $x=L$). Then, using the resulting water motion, the sediment concentration for the (nonextended) domain of interest is calculated. The suspended sediment concentration at the seaward boundary of the physical domain (C_m) is prescribed to be a constant. The value of C_m is determined by prescribing the averaged sediment availability a_s in the physical domain

$$a_s = \frac{\int_0^L \int_{y_1}^{y_2} a \, dy dx}{\int_0^L \int_{y_1}^{y_2} dy dx} \quad (26)$$

to be constant, such that a maximum residual SSC of $\sim 200 \text{ mg L}^{-1}$ representative for the observed ETM in the Delaware estuary under a relatively small river discharge ($\sim 288 \text{ m}^3 \cdot \text{s}^{-1}$; see McSweeney et al., 2016b) is obtained.

The vertical eddy viscosity A_v is assumed to be constant in time. Both A_v and the slip parameter s are assumed to be proportional to the local water depth (Friedrichs & Hamrick, 1996; Wei et al., 2017),

$$A_v = A_{v_m} \frac{H}{H_m}, \quad s = s_m \frac{H}{H_m}. \quad (27)$$

Here H_m is the width-averaged water depth, A_{v_m} and s_m are prescribed friction parameters which are obtained from calibrating the M_2 tidal water motion with observations in the Delaware estuary (values taken from Wei et al., 2016). Using these parameter settings, the leading-order tidal surface elevation obtained from the present 3-D model is nearly the same as that obtained in their width-averaged model. The model qualitatively reproduces the observed M_2 tidal surface elevation and the three-dimensional flow structures due to barotropic flow components and gravitational circulation. A discussion of the model performance on the water motion and salinity (transport) can be found in Wei et al. (2017), and is not repeated in this paper. The Delaware estuary is characterized by sediments of different grain-sizes which are distributed at different locations (Biggs & Church, 1984; Gibbs et al., 1983). For simplicity, a constant settling velocity value is used in the default experiment: $w_s = 0.5 \text{ mm} \cdot \text{s}^{-1}$, representative for sediments in the lower Delaware Bay. To investigate the sediment dynamics for sediments of different settling velocities, two other settling velocities will be considered ($w_s = 0.2 \text{ mm} \cdot \text{s}^{-1}$, $1 \text{ mm} \cdot \text{s}^{-1}$) in the sensitivity study (see section 5.1). The grain size of sediments, the mean water density, and sediment density are also assumed to be constant: $d_s = 20 \text{ } \mu\text{m}$, $\rho_0 = 1,020 \text{ kg} \cdot \text{m}^{-3}$, $\rho_s = 2,650 \text{ kg} \cdot \text{m}^{-3}$. For clarity, the Coriolis force is neglected in the default experiment, its effect will be discussed in detail in section 4. All above-mentioned parameters defining the default experiment are listed in Table 2.

Table 2
Parameters for the Default Experiment

Physical Parameter	Symbol	Value
Length	L	215 km
Convergence length	L_b	42 km
Width at the mouth	B_0	39 km
Minimum water depth	H_{\min}	3.6 m
Maximum water depth	H_{\max}	15 m
Average water depth	H_m	8 m
Tidal flat parameter	C_f	4
Average vertical eddy viscosity	$A_{v,m}$	$0.005 \text{ m}^2 \cdot \text{s}^{-1}$
Average slip parameter	S_m	$0.039 \text{ m} \cdot \text{s}^{-1}$
Horizontal diffusivity	K_h	$10\text{--}50 \text{ m}^2 \cdot \text{s}^{-1}$
River discharge	Q	$288 \text{ m}^3 \cdot \text{s}^{-1}$
Average M_2 tidal amplitude	$a_{M_2}^m$	0.75 m
Average M_4 tidal amplitude	$a_{M_4}^m$	0.012 m
Average residual water level	$a_{M_0}^m$	0
M_2 tidal frequency	σ_{M_2}	$1.4 \times 10^{-4} \text{ s}^{-1}$
Average phase difference	$\Delta\phi^m$	-247°
Coriolis parameter	f	0
Salinity at the mouth	S_m	31 psu
Mean water density	ρ_0	$1,020 \text{ kg} \cdot \text{m}^{-3}$
Sediment grain size	d_s	20 μm
Sediment density	ρ_s	$2,650 \text{ kg} \cdot \text{m}^{-3}$
Settling velocity	w_s	$0.5 \text{ mm} \cdot \text{s}^{-1}$
Average sediment availability	a_s	0.1228

3.2. Three-Dimensional Suspended Sediment Concentration

Since no Coriolis force is considered, and the bed profile and geometry are laterally symmetric, the sediment availability and sediment concentrations are symmetric with respect to the central axis of the estuary ($y = 0$). As shown in Figure 3a, the maximum sediment availability is found at about 100 km up-estuary from the mouth, with larger values on the shoals than in the deeper channel. To illustrate the three-dimensional structure of the ETM and its position with respect to the tidally averaged salinity structure, the longitudinal-vertical distribution of the residual suspended sediment concentration at $y = 0$ and a lateral-vertical (cross-sectional) distribution within the ETM region (at $x = 100$ km) are depicted in Figures 3b and 3c. The residual salinity distributions are vertically uniform (see white lines), however, the residual suspended sediment concentrations are generally larger near the bottom than near the top (see color scales). The ETM is centered at ~ 100 km, with the turbidity zone stretching between 55 km and 130 km from the mouth (see Figure 3b). The maximum residual suspended sediment concentration is found at a salinity of about 0.05 psu, coinciding with the residual salt intrusion limit. Due to larger sediment availabilities on the shoals and larger residual salinities in the deeper channel (see Figure 3c), the residual suspended sediment concentrations are larger on the shoals than in the deeper channel (even though the bed shear stress in the deeper channel is larger). The lateral distributions of the residual salinity and suspended sediment concentration confirm the results of Huijts et al. (2006), that salinity gradients tend to trap sediment in regions of the cross section with lower salinities.

3.3. Depth-Integrated Sediment Transport and Trapping Mechanisms

To identify the longitudinal and lateral sediment transport patterns and the depth-averaged sediment trapping patterns, the depth-integrated residual sediment transport and the depth-averaged residual sediment concentration are shown in Figure 4. The maximum depth-averaged residual sediment concentration is located at $x = 100$ km, with the depth-averaged ETM region extending from 70 to 120 km up-estuary from the mouth. Four circulation cells of residual sediment transport are identified (see arrows in Figure 4): seaward of the ETM, sediments are transported toward the ETM through the deeper channel, next move laterally toward the flanks and are transported seaward over the shoal; within the ETM region, sediments are transported seaward through the deeper channel and landward over the shoals. The longitudinal residual sediment flux (integrated over the depth) reaches its maximum (up to $24 \text{ g m}^{-1} \text{ s}^{-1}$) in the deeper channel

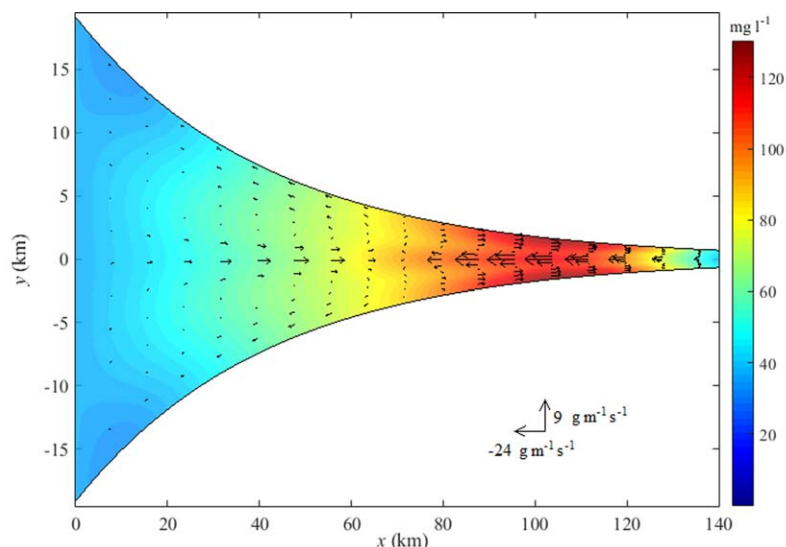


Figure 4. The depth-averaged residual suspended sediment concentration (see background color scales) and the depth-integrated sediment flux (see arrows). The length of the arrow measures the magnitudes of the depth-integrated residual suspended sediment flux at each location (x, y) , and the direction of the arrow measures the direction of the flux at this location.

sediment transport in the deeper channel (see Figure 4) is mainly due to \mathbf{T}_{M_0} and tidal pumping, while the seaward sediment transport over the shoals is predominantly controlled by \mathbf{T}_{M_0} .

To assess the relative importance of the advection of residual sediment concentrations by gravitational circulation ($\mathbf{T}_{M_0}^{GC}$) and the other barotropic residual currents ($\mathbf{T}_{M_0}^{BR}$), the sediment transport due to these two contributions is shown in Figures 5d and 5e, respectively, together with the resulting divergence of the transport. It is found that the largest contribution to the divergence of the residual sediment transport \mathbf{T}_{M_0} in the seaward side of the ETM is related to the advection of the residual concentrations by the gravitational circulation ($\mathbf{T}_{M_0}^{GC}$). The convergence of the residual sediment transport \mathbf{T}_{M_0} on the shoals downstream of the ETM is due to the combined effects of $\mathbf{T}_{M_0}^{GC}$ and $\mathbf{T}_{M_0}^{BR}$. The convergence of the residual sediment transport \mathbf{T}_{M_0} in the ETM region, however, is mainly resulting from the advection of residual concentrations by the barotropic residual currents ($\mathbf{T}_{M_0}^{BR}$) (see Figure 5e). The transport contribution $\mathbf{T}_{M_0}^{GC}$ tends to transport sediments landward through the deeper channel and seaward over the shoals (see Figure 5d). The contribution $\mathbf{T}_{M_0}^{BR}$, however, transports sediments seaward at each location, especially in the deeper channel. In the deeper channel downstream of the ETM, the landward residual sediment transport contribution $\mathbf{T}_{M_0}^{GC}$ exceeds the seaward transport contribution $\mathbf{T}_{M_0}^{BR}$, while on the shoals, both $\mathbf{T}_{M_0}^{GC}$ and $\mathbf{T}_{M_0}^{BR}$ contribute to a seaward sediment transport. As a result, the landward sediment transport contribution \mathbf{T}_{M_0} in the deeper channel is smaller than the seaward transport on the shoals, as shown in Figure 5a.

3.4. Cross-Sectionally Integrated Residual Sediment Balance

Integrating the sediment transport over the cross section results in the cross-sectionally integrated residual sediment transport balance due to different mechanisms. In Figure 6a, it is shown that T_{M_2} and T_{M_0} are the dominant landward and seaward residual sediment transport contributions, respectively, while the residual sediment transport contributions T_{M_4} and T_{DIFF} are much smaller. This implies the dominant sediment transport processes are well-resolved by the idealized model. Since the horizontal diffusion tends to spread out sediments from the ETM, reducing horizontal diffusivity may slightly decrease the width of the ETM. To obtain the dominant sediment importing and exporting mechanisms, the sediment transport contributions T_{M_2} and T_{M_0} are further decomposed into contributions related to specific mechanisms listed in Table 1. The largest contribution to the landward residual sediment transport contribution T_{M_2} is caused by the M_2 tidal advection of the suspended sediment concentrations at the M_2 tidal frequency ($T_{M_2}^{IN}$), as a result of the asymmetric bed shear stress due to interactions of the M_2 bottom velocity and the internally generated M_4 bottom velocity. The M_2 tidal advection of the M_2 tidal concentration as a result of the spatial settling lag

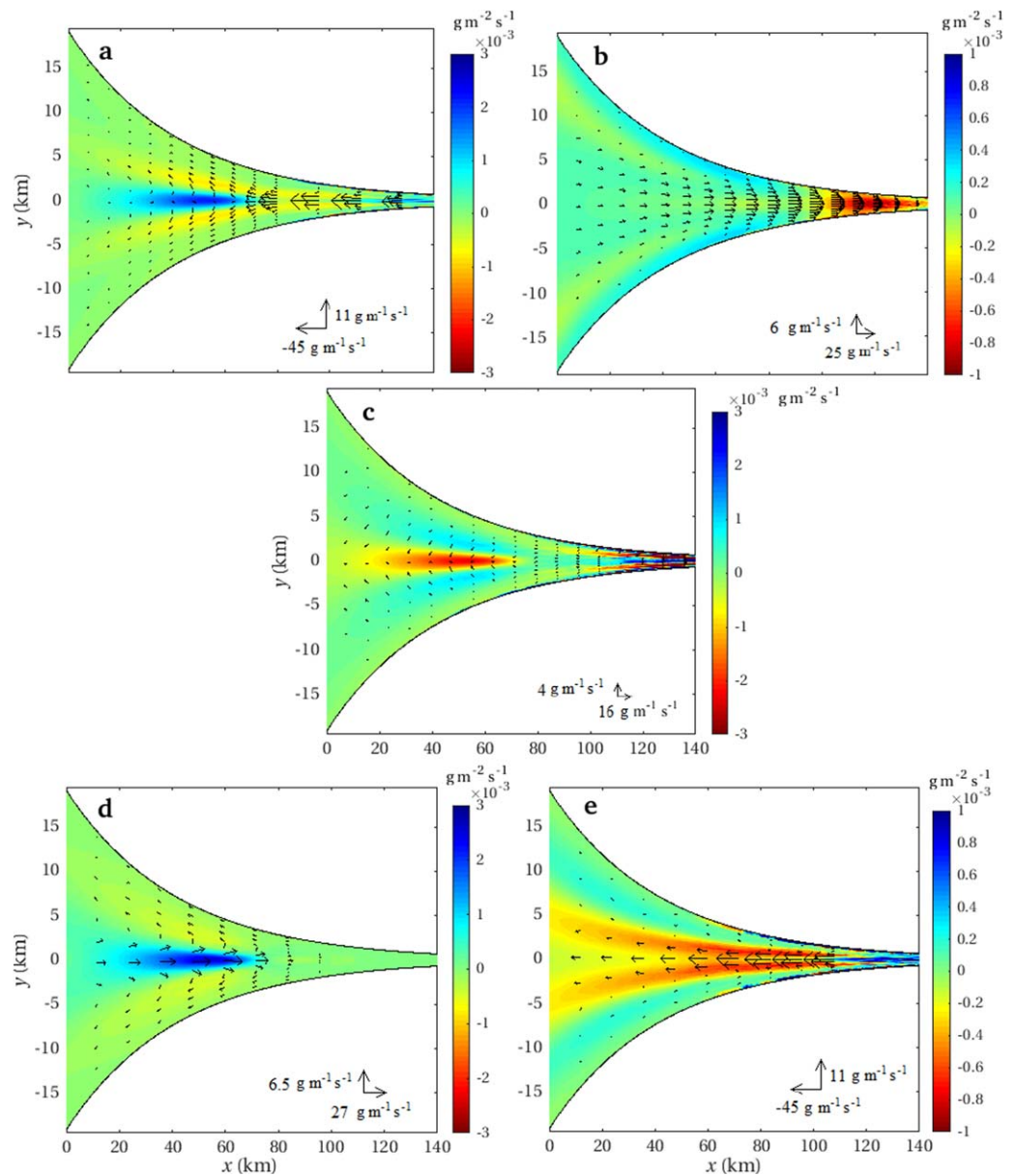


Figure 5. The divergence of the depth-integrated residual sediment transport (see color scales) due to (a) residual advection of residual concentrations (T_{M_0}), (b) tidal pumping ($T_{M_2} + T_{M_4}$), (c) diffusion (T_{DIFF}), (d) transport due to advection of residual suspended sediment concentration by gravitational circulation ($T_{M_0}^{GC}$), and (e) barotropic residual currents ($T_{M_0}^{BR}$). The directions and magnitudes of the transport vectors are shown by arrows.

effects also results in a significant landward residual sediment transport contribution ($T_{M_2}^{SSL}$). The tidal advection of the tidal concentrations as a result of the asymmetric bed shear stress due to the combined salinity-induced bottom residual velocity and the M_2 bottom flow also contributes to a small but nonnegligible landward sediment transport ($T_{M_2}^{GC}$). The M_2 tidal advection of the M_2 tidal concentration as a result of the asymmetric bed shear stress due to interactions between the M_2 tidal velocities and the externally generated M_4 tidal velocities ($T_{M_2}^{EF}$), however, is negligible for the residual sediment balance integrated over the cross section. The M_2 tidal advection of the M_2 tidal concentration as a result of the asymmetric bed shear stress due to interactions between the M_2 tidal velocities and the barotropic residual currents ($T_{M_2}^{BR}$) and transport due to surface contribution ($T_{M_2}^{SC}$) result in a seaward residual transport of sediment. In Figure 6c, it is shown that the advection of the residual sediment concentration by gravitational circulation ($T_{M_0}^{GC}$) contributes to a landward sediment transport. The advection of residual sediment concentration by all

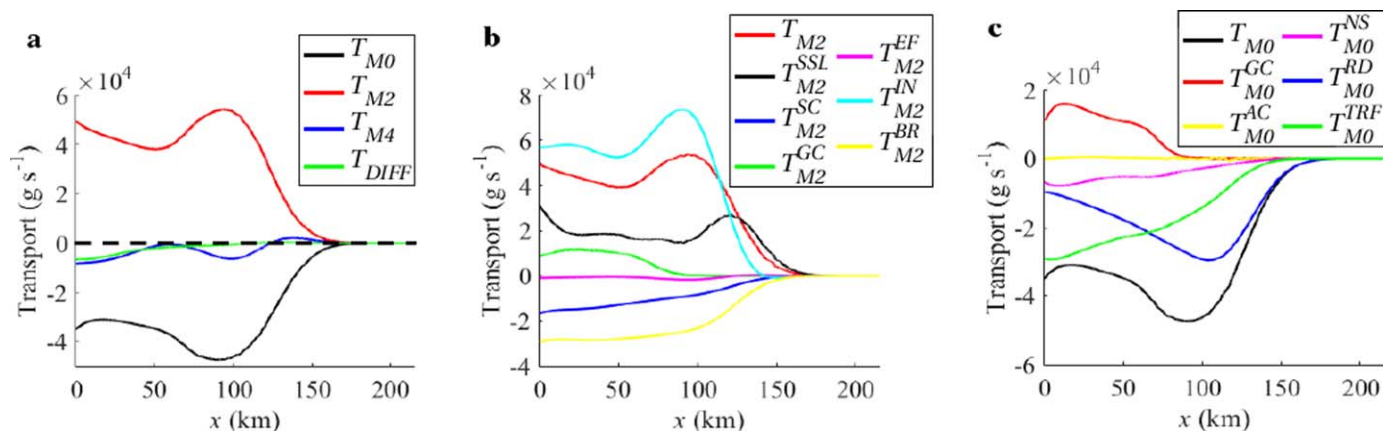


Figure 6. (a) Cross-sectionally integrated residual sediment transport contributions T_{M_0} , T_{M_2} , T_{M_4} , and T_{DIFF} . Decomposed cross-sectionally integrated sediment transport contributions of (b) T_{M_2} and (c) T_{M_0} .

barotropic residual velocities ($T_{M_0}^{RD}$, $T_{M_0}^{AC}$, $T_{M_0}^{NS}$, $T_{M_0}^{TRF}$), however, result in a seaward sediment transport contribution (see Figure 6c), with $T_{M_0}^{RD}$ and $T_{M_0}^{TRF}$ the dominant seaward sediment transport contributions.

3.5. Contributions to the ETM

In this section, the significance of residual sediment transport contributions due to M_2 tidal advection of the M_2 tidal concentration related to the internally generated M_4 overtide, spatial settling lag effects, and the residual and M_2 tidal advective transport by gravitational circulation to the ETM formation is studied. Three dedicated experiments, in which one of these contributions is excluded, are used to show the differences of the characteristics of the resulting ETM in comparison with those in the default experiment. In these experiments, the sediments within the estuary have to be redistributed to reach a new morphodynamic equilibrium, resulting in a changed sediment availability distribution and thus an altered ETM.

In experiments 1–2, the sediment transport contributions related to the internally generated M_4 overtide ($T_{M_2}^{IN}$) and the spatial settling lag effects ($T_{M_2}^{SSL}$) are excluded, respectively. In both experiments, the ETM moves to the seaward boundary (see Figures 7a and 7b). This implies that both $T_{M_2}^{IN}$ and $T_{M_2}^{SSL}$ are essential for the sediment trapping and the occurrence of the ETM in the central estuary. In experiment 3, the transport contribution related to gravitational circulation ($T_{M_2}^{GC} + T_{M_0}^{GC}$) is excluded. Compared to the default experiment, the longitudinal location of the ETM is hardly changed, but the residual sediment concentration is reduced in the ETM (less than 90 mg L^{-1}), see Figure 7c. This implies that even though the residual sediment transport contribution involving gravitational circulation results in a much more efficient trapping of sediments in the ETM and thence a much larger maximum sediment concentration (up to 130 mg L^{-1} , see Figure 4), it is not essential for the formation of the ETM in the central estuary. It is worth noting that, by excluding this contribution, the sediment concentrations become larger in the deeper channel than on the shoals in the downstream region. In conclusion, the sediment transports related to gravitation circulation play an important role in redistributing the trapped sediments in both longitudinal and lateral directions.

4. Influence of Coriolis Deflection

To investigate the influence of earth rotation on the sediment distribution and trapping (necessary to compare the results with observations in the Delaware estuary), the Coriolis force is included in a dedicated experiment with $f = 1 \times 10^{-4} \text{ rad s}^{-1}$. Comparing Figure 8a with Figure 3a shows that the location of the maximum sediment availability ($\sim 100 \text{ km}$ from the seaward boundary) is unchanged by the Coriolis force. The sediment availability, however, becomes laterally asymmetric, with larger values on the right shoal than on the left, looking seaward. In Figures 8b and 8c, the 2DV distributions of the residual SSC and isohalines at the central axis of the estuary and their cross-sectional distribution at $x = 100 \text{ km}$ are shown, respectively. Comparing Figures 8b and 8c with Figures 3b and 3c reveals that the inclusion of the Coriolis forcing hardly change the longitudinal and vertical patterns of the residual SSC or salt intrusion (though the magnitudes of the residual SSC and salinity are slightly changed), but the lateral patterns of both the residual SSC and

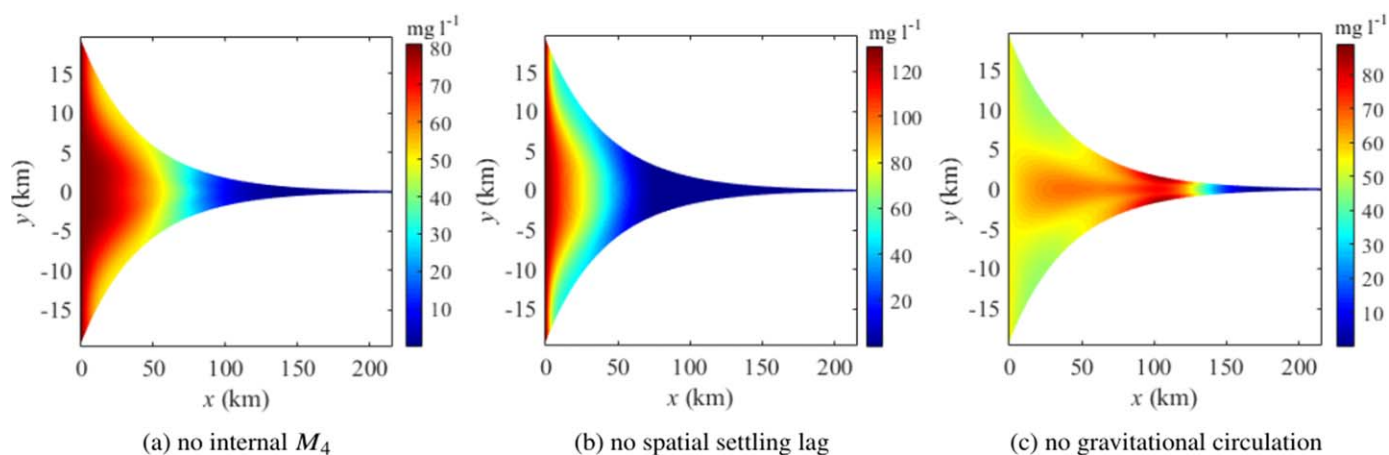


Figure 7. The depth-averaged residual suspended sediment concentration after excluding the sediment transport contributions due to (a) the internally generated M_4 overtide, (b) the spatial settling lag effects, and (c) the gravitational circulation, respectively.

salinity are significantly changed. The Coriolis effects result in larger residual salinities on the left side of the estuary than on the right (see white lines in Figure 8c). These lateral salinity gradients contribute to a lateral gravitational circulation transporting sediments from the left side of the estuary to the right side, thus resulting in larger sediment concentrations on the right shoal than on the left shoal, see Figure 8c. This lateral sediment trapping pattern in relation to the lateral salinity gradients is again consistent with results in Huijts et al. (2006). Figure 8d shows that the depth-integrated sediment transport patterns are significantly changed by the Coriolis force: sediments are transported landward from the left side of the estuary and transported seaward from the right side. The depth-integrated residual sediment flux in both longitudinal and lateral directions are increased, with the maximum longitudinal sediment transport of $35 \text{ g m}^{-1} \text{ s}^{-1}$ on the right shoal in the ETM region and a maximum lateral sediment transport of up to $\sim 5 \text{ g m}^{-1} \text{ s}^{-1}$ on the left side of the deeper channel near the mouth. The relative importance of different mechanisms for the depth-integrated and cross-sectionally integrated residual sediment transport is hardly changed by Coriolis deflection (not shown).

Due to the lack of field data for the sediment availability in the Delaware estuary, the quality of the simulated sediment availability a can not be directly measured. Nevertheless, since the SSC and a are strongly related (following equations (13) and (14)), the reliability of a can be assessed by comparing the simulated SSC's to observations. It is found that the main features of the ETM in the Delaware estuary observed by McSweeney et al. (2016b) are qualitatively reproduced. First of all, the ETM is centered around 100 km for the river discharge used here ($288 \text{ m}^3 \cdot \text{s}^{-1}$), with the region of elevated SSC distributed between approximately 80 km and 120 km from the mouth. Secondly, the lateral distribution of the simulated SSC is also consistent with observations, with larger sediment concentrations at the Delaware (right) side of the estuary than at the New Jersey (left) side. Beyond that, the region with the highest sediment availability (on the right shoals, see Figure 8a) coincides well with the area where most fine sediments are observed (Biggs & Church, 1984). Therefore, it is reasonable to believe the simulated a for the sediments considered in this experiment is realistic. Moreover, the spatial sediment transport patterns observed by McSweeney et al. (2016b) are qualitatively reproduced, with sediments transported into the estuary from the left side of the deep channel, and transported down-estuary on the right flanks. The model also confirms that the lateral depth-integrated residual sediment transport is mainly due to the advection of the residual SSC by the residual currents, while sediment transport contributions due to both tidal pumping and residual advection of residual concentration contribute significantly to the longitudinal residual sediment transport.

5. Sensitivity to Sediment Grain Size and River Discharge

To investigate the sensitivity of the sediment trapping locations and mechanisms to particle size and river discharge, four experiments considering different grain sizes and river discharges are performed. In section 5.1, the sensitivity to the sediment grain size is studied by considering a grain size of $10 \mu\text{m}$ (fine-grained

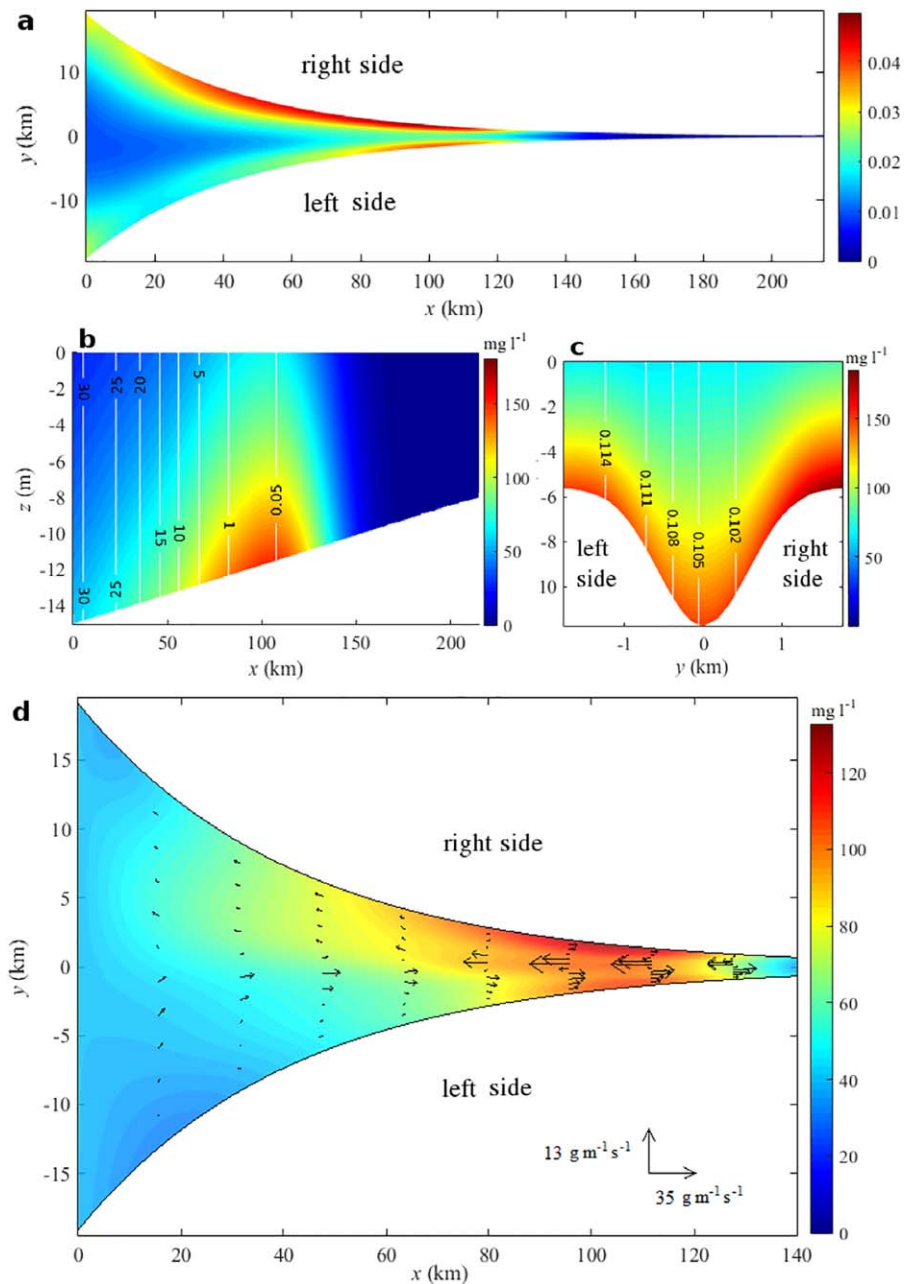


Figure 8. Same as Figures 3 and 4, but for $f=1 \times 10^{-4}$ rad s⁻¹.

sediments) and 40 μm (relatively coarse-grained sediments), corresponding to a settling velocities of $w_s=0.2$ mm·s⁻¹ and $w_s=1$ mm·s⁻¹ (Fredsoe & Deigaard, 1992), respectively. The settling velocity 0.2 mm·s⁻¹ (for the first sensitivity experiment) is at the lower limit of those used for the Hudson River estuary (Ralston et al., 2013), and may be not typical in the Delaware estuary. Nevertheless, the sensitivity experiments aim to investigate the influence of the sediment settling velocity on the sediment transport/trapping mechanisms, and will provide useful insight into the spatial sorting of sediments of different grain-sizes observed in many estuaries. In section 5.2, the sensitivity to river discharge is investigated considering two different river discharges, $Q = 72$ m³·s⁻¹, 864 m³·s⁻¹. In these experiments, all other parameters including the averaged sediment availability a_{*f} are the same as those used in the default experiment. The differences of the sediment trapping and residual transport patterns, and the relative importance of different mechanisms to the ETM formation, will be discussed in comparison with those in the default experiment.

5.1. Sensitivity to Sediment Grain Size

5.1.1. Fine-Grained Sediments

As found in the default experiment, the sediment availabilities for very fine sediments ($w_s=0.2 \text{ mm}\cdot\text{s}^{-1}$, $d_s=10 \text{ }\mu\text{m}$) are larger on the shoals than in the channel, consistent with the observations in the Delaware Bay (Biggs & Church, 1984) as fine sediments are mostly found on the shoals. By considering more fine-grained sediments, the sediment availability, the three-dimensional structure of the residual SSC, and the depth-integrated sediment transport patterns change significantly (see Figure 9) compared to those in the default experiment. The maximum sediment availability moves toward the seaward side, and is found at $x \approx 30 \text{ km}$ (see Figure 9a). The residual SSC becomes more vertically uniform, and the ETM occurs at relatively large salinities in the downstream region (see Figure 9b). Moreover, the lateral difference of the residual SSC between the shoals and the deeper channel becomes more pronounced, with more strongly elevated residual sediment concentrations on the shallow shoals at all depths (Figure 9c). In the region with elevated depth-averaged residual sediment concentrations ($x < 70 \text{ km}$), the depth-integrated residual sediment transport circulation cells are enhanced with a significant landward transport through the deeper channel and seaward transports over the shoals (see Figure 9d).

The cross-sectionally integrated residual transport contributions T_{M_2} and T_{M_0} remain the dominant sediment transport contributions (Figure 10a), but the transport mechanisms are significantly changed (Figures 10b and 10c) compared to the default experiment. The sediment transport contributions due to the M_2 tidal advection of M_2 tidal concentrations related to the internally generated M_4 overtide ($T_{M_2}^{\text{IN}}$) and the gravitational circulation ($T_{M_2}^{\text{GC}}$) are both reduced, while that related to spatial settling lag effects ($T_{M_2}^{\text{SSL}}$) is significantly increased (Figure 10b). The transport due to advection of residual SSC by gravitational circulation $T_{M_0}^{\text{GC}}$ results in a significant seaward sediment transport for fine-grained sediments (Figure 10c), contrasting the landward transport contribution $T_{M_0}^{\text{GC}}$ in the default experiment (Figure 6c).

The contribution of the sediment transports related to the internally generated M_4 tide ($T_{M_2}^{\text{IN}}$), spatial settling lag effects ($T_{M_2}^{\text{SSL}}$) and gravitational circulation ($T_{M_2}^{\text{GC}} + T_{M_0}^{\text{GC}}$) to the trapping patterns of fine-grained sediments are strongly influenced by the sediment grain-size. For fine-grained sediments, excluding the sediment transport contributions caused by the spatial settling lag effects and the internally generated M_4 overtide results in an ETM at the seaward boundary (Figures 10a and 10b), as was found in the default experiment. However, different from the default experiment, excluding the sediment transport contribution induced by gravitational circulation, results in a noticeable landward shift of the ETM (up to $\sim 30 \text{ km}$, see Figure 10c). This again illustrates that gravitational circulation plays an important role in seaward sediment transport and in trapping fine-grained sediments in the downstream region.

5.1.2. Coarse-Grained Sediments

For more coarse-grained sediments ($w_s = 1 \text{ mm}\cdot\text{s}^{-1}$, $d_s=40 \text{ }\mu\text{m}$), the longitudinal locations of the maximal sediment availability a hardly changes compared to the default experiment, but the maximum a is now found in the deeper channel (see Figure 11a). This tendency is also consistent with Biggs and Church (1984) who found most coarse sediments in the central channel of the Delaware Bay. The longitudinal location of the maximum residual SSC is nearly the same as that in the default experiment (coinciding with the ~ 0.05 psu isohaline, see Figure 11b). Considering a larger settling velocity, however, results in a much larger residual SSC near the bottom than in the upper layers. The larger settling velocity also results in much stronger lateral SSC gradients for coarse sediments than those for fine sediments (due to reduced lateral exchange of sediment), with much higher SSC's in the channel than on the shoals (see Figure 11c). The depth-integrated residual transport of coarse-grained sediments is most significant in the ETM region between 70 km and 120 km up-estuary from the mouth (see color scales in Figure 11d), where sediments are efficiently transported seaward through the deeper channel and landward over the shoals (see arrows).

By considering sediments of a larger grain size, the landward transport contribution due to M_2 tidal advection of the M_2 tidal concentrations related to the internally generated M_4 overtide ($T_{M_2}^{\text{IN}}$) becomes more significant, while that related to spatial settling lag effects ($T_{M_2}^{\text{SSL}}$) decreases within the ETM region and contributes to a seaward transport of sediments downstream of the ETM (for $x < 70 \text{ km}$). The landward sediment transport contributions due to advective transport by gravitational circulation ($T_{M_2}^{\text{GC}}$ and $T_{M_0}^{\text{GC}}$) are increased, see Figures 12b and 12c. These transport contribution changes have a strong influence on the ETM: the ETM shifts seaward (for $\sim 30 \text{ km}$) by excluding the M_2 tidal advection of M_2 tidal concentrations related to the internally generated M_4 tide (Figure 12d); excluding the contribution related to the spatial

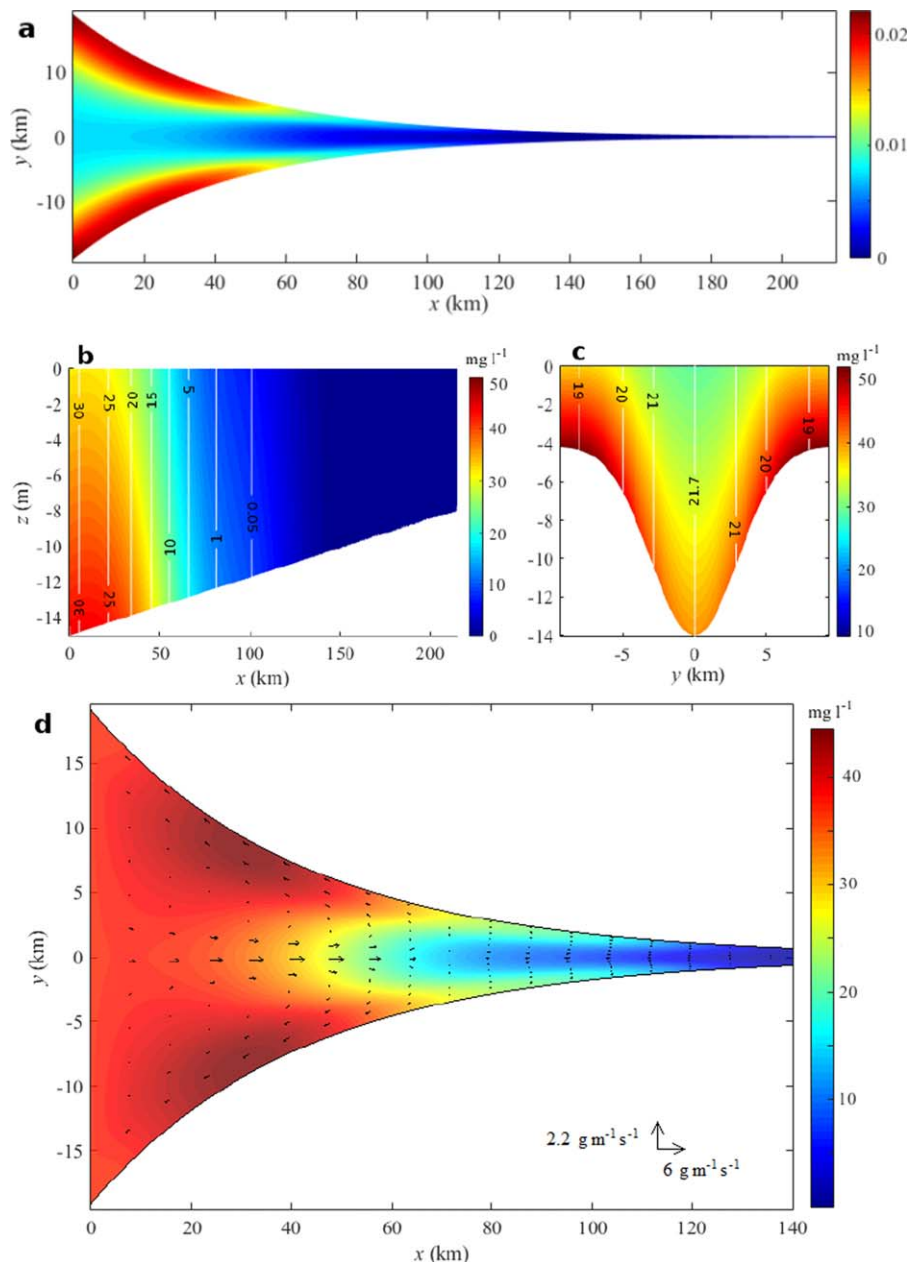


Figure 9. Same as Figure 8, but for $f = 0$, $w_s = 0.2 \text{ mm} \cdot \text{s}^{-1}$ and $d_s = 10 \mu\text{m}$. The cross section in Figure 9c is taken at $x = 30 \text{ km}$.

settling lag effects also results in a seaward shift of the ETM (for $\sim 20 \text{ km}$), and the width of the region with elevated concentrations significantly decreases (Figure 12e). Excluding the residual sediment transport due to advection of residual SSC by gravitational circulation results in an ETM near the seaward boundary (Figure 12f).

The changes of the relative importance of the main cross-sectionally integrated residual sediment transport contributions are summarized in Table 3. Here “+” indicates the importance of the transport contribution is increased compared to that in the default experiment, “-” indicates the contribution becomes less important, and “*” indicates that the direction of the sediment transport contribution is changed. The qualitative changes (relative importance) of these transport contributions are mainly related to different settling velocities. By considering more fine-grained sediments with smaller settling velocities, it allows particles to travel longer distances in both longitudinal and lateral directions before settling to the bottom, which results in a more important

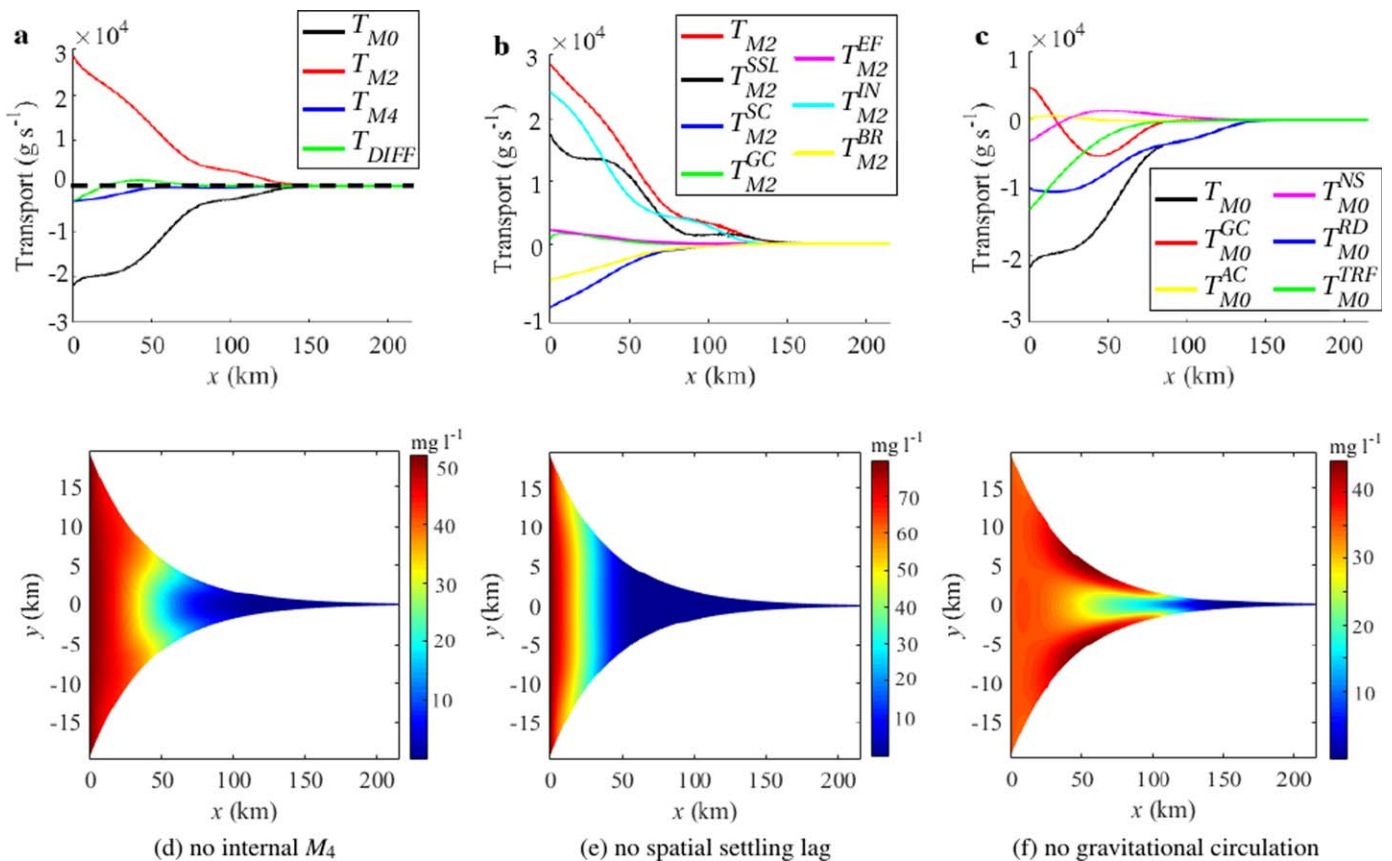


Figure 10. Same as (top) Figure 6 and (bottom) Figure 7, but for $w_s = 0.2 \text{ mm} \cdot \text{s}^{-1}$ and $d_s = 10 \text{ } \mu\text{m}$.

sediment transport contribution due to the spatial settling lag effects ($T_{M_2}^{SSL}$). Smaller settling velocities are also responsible for a more uniform suspended sediment concentration over the cross section (see for example Figure 9c). This results in less important contributions due to advection of residual SSC by residual circulation ($T_{M_0}^{GC}$, $T_{M_0}^{NS}$, $T_{M_0}^{TRF}$), and less important contributions due to tidal advection of tidal concentrations related to asymmetric bed shear stresses ($T_{M_2}^{GC}$, $T_{M_2}^{BR}$, $T_{M_2}^{IN}$), as shown in Table 3. The advection of residual SSC by river-induced flow ($T_{M_0}^{RD}$) becomes more dominant in the seaward residual sediment transport as a result of the increased residual SSC in the upper water column where the maximum river-induced flow occurs. The seaward residual transport due to advection of residual SSC by gravitational circulation integrated over the cross section ($T_{M_0}^{GC}$) is caused by much larger residual concentrations on the shoals than in the deeper channel, and the seaward residual sediment transport on the shoals exceeds the landward transport in the deeper channel.

By considering a larger sediment grain size with larger settling velocity, sediments can settle to the bed faster, resulting in a more concentrated region near the bottom of the deeper channel (see Figure 11c), where the bed shear stress is largest. As a result, the residual sediment transport contribution related to the spatial settling lag effects ($T_{M_2}^{SSL}$) becomes less important, and a seaward residual sediment transport is induced downstream of the ETM. The residual sediment transport contributions related to the advection of residual SSC by residual circulation ($T_{M_0}^{GC}$, $T_{M_0}^{NS}$, $T_{M_0}^{TRF}$) and the M_2 tidal advection of M_2 tidal concentrations related to asymmetric bed shear stress ($T_{M_2}^{GC}$, $T_{M_2}^{BR}$, $T_{M_2}^{IN}$), however, become more important (see Table 3). The sediment transport contribution $T_{M_0}^{RD}$ is decreased because of the reduced surface concentration.

5.2. Sensitivity to River Discharge

5.2.1. Low River Discharge

By decreasing the river discharge from 288 to $72 \text{ m}^3 \cdot \text{s}^{-1}$, the largest sediment availability moves landward by $\sim 30 \text{ km}$, and is now located at $x \sim 130 \text{ km}$ (Figure 13a). The residual salt intrusion at

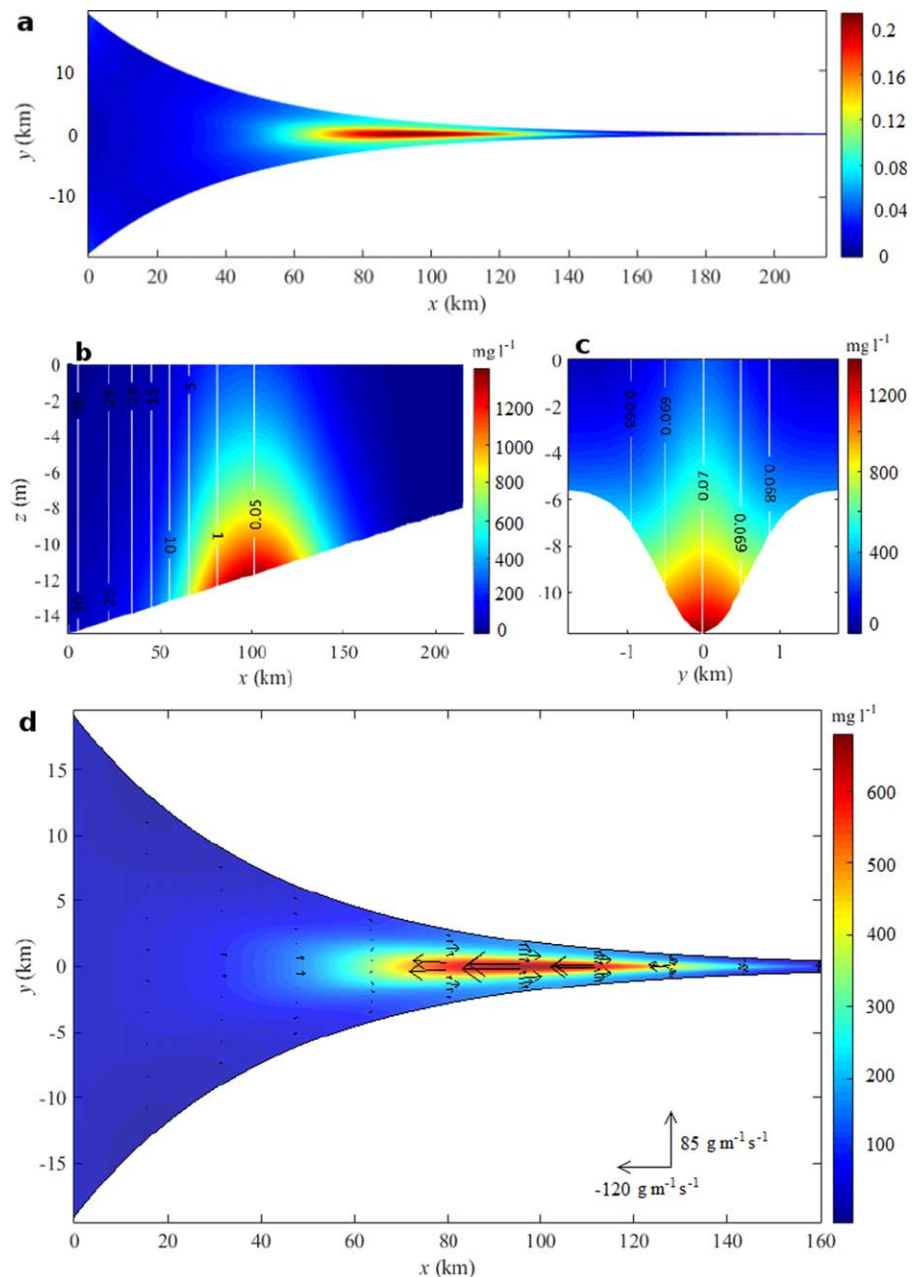


Figure 11. Same as Figure 8, but for $w_s = 1 \text{ mm} \cdot \text{s}^{-1}$ and $d_s = 40 \text{ } \mu\text{m}$. The cross section in Figure 11c is taken at $x = 100 \text{ km}$.

the central axis of the estuary is enhanced, reaching its landward limit at $\sim 130 \text{ km}$ up-estuary from the mouth, where the maximum residual suspended sediment concentration is found (Figure 13b). At the cross section at $x = 130 \text{ km}$, salinities are larger in the deeper channel than on the shoals, and the residual sediment concentrations are larger on the shoals than in the middle of the channel (Figure 13c). The depth-integrated residual sediment transport is significantly reduced, with a small seaward sediment transport through the deeper channel and landward transport over the shoals within the ETM region (Figure 13d).

By decreasing the river discharge, T_{M_2} and T_{M_0} remain the most dominant sediment transport contributions integrated over the cross section (Figure 14a). The dominance of sediment transport contribution related to the internally generated M_4 overtide ($T_{M_2}^{\text{IN}}$) becomes more pronounced, and the transport due to the spatial settling lag effects ($T_{M_2}^{\text{SSL}}$) results in a more important landward sediment transport downstream of the ETM

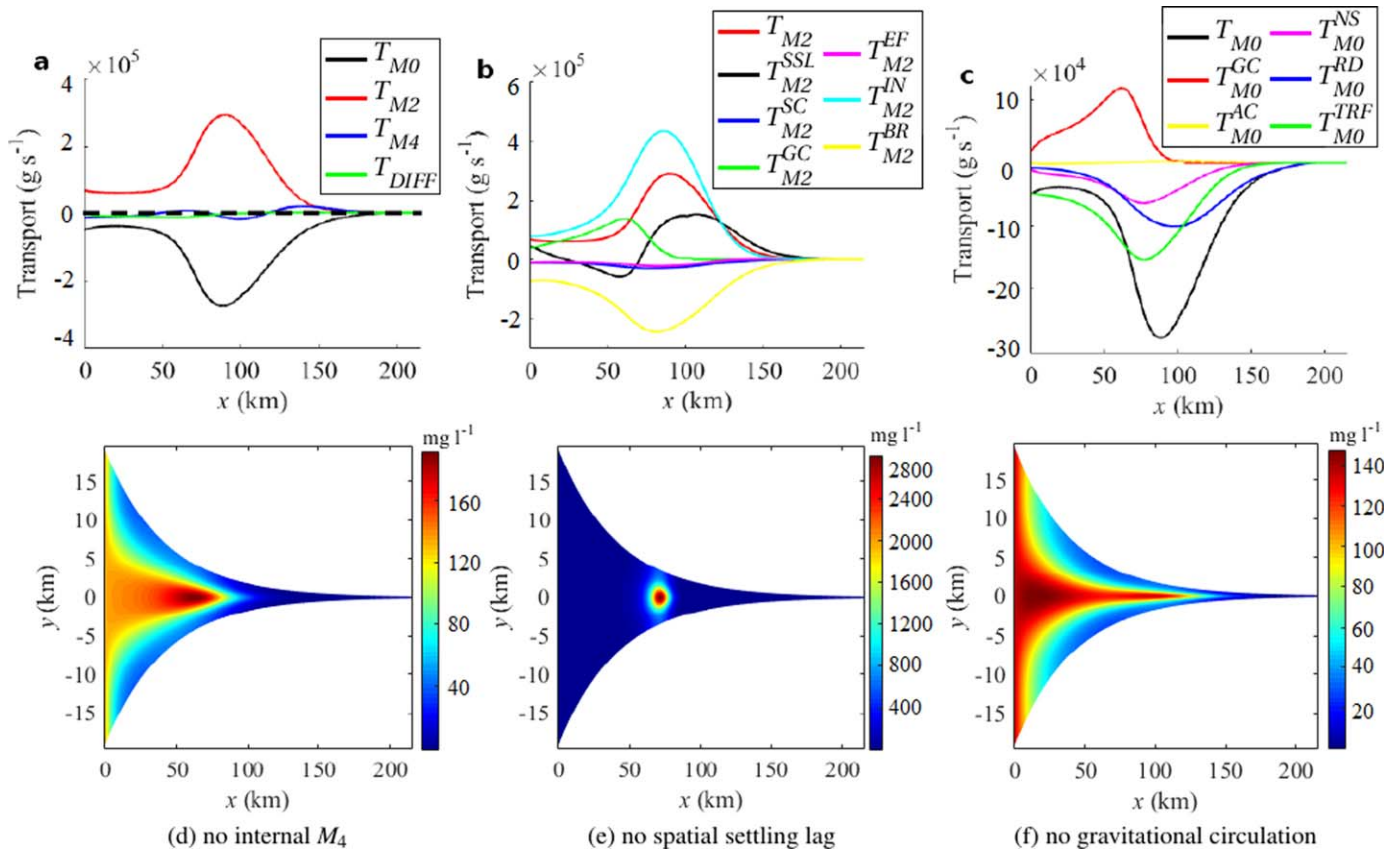


Figure 12. Same as (top) Figure 6 and (bottom) Figure 7, but for $w_s = 1 \text{ mm}\cdot\text{s}^{-1}$ and $d_s = 40 \mu\text{m}$.

and seaward transport upstream of the ETM. The sediment transports due to both river discharge ($T_{M_0}^{\text{RD}}$) and gravitational circulation ($T_{M_0}^{\text{GC}}$ and $T_{M_2}^{\text{GC}}$) decrease significantly (see Figures 14b and 14c).

Excluding the M_2 tidal advection of the M_2 tidal component of concentrations related to the internally generated M_4 tide results in a seaward shift of the ETM from the central estuary to the mouth (see Figure 14a). By excluding the sediment transport due to the spatial settling lag effects, the ETM slightly shifts toward the

Table 3

Changes of the Relative Importance of Main Residual Sediment Transport Contributions Integrated Over the Cross Section by Varying Settling Velocities and River Discharges

Transport	Decomposition	$w_s = 0.2 \text{ mm}\cdot\text{s}^{-1}$ $d_s = 10 \mu\text{m}$	$w_s = 1 \text{ mm}\cdot\text{s}^{-1}$ $d_s = 40 \mu\text{m}$	$Q = 72 \text{ m}^3\cdot\text{s}^{-1}$	$Q = 864 \text{ m}^3\cdot\text{s}^{-1}$
T_{M_2}	$T_{M_2}^{\text{GC}}$	-	+	-	+
	$T_{M_2}^{\text{BR}}$	-	+	-	+
	$T_{M_2}^{\text{IN}}$	-	+	+	-
	$T_{M_2}^{\text{SSL}}$	+	*	*	+
T_{M_0}	$T_{M_0}^{\text{GC}}$	*	+	-	+
	$T_{M_0}^{\text{NS}}$	-	+	+	-
	$T_{M_0}^{\text{TRF}}$	-	+	+	-
	$T_{M_0}^{\text{RD}}$	+	-	-	+

Note. Here “+” and “-” indicate the relative importance of the sediment transport contribution is increased and decreased, respectively, and “*” indicates the resulting residual sediment transport changes from a seaward transport contribution to a landward transport contribution, or vice versa.

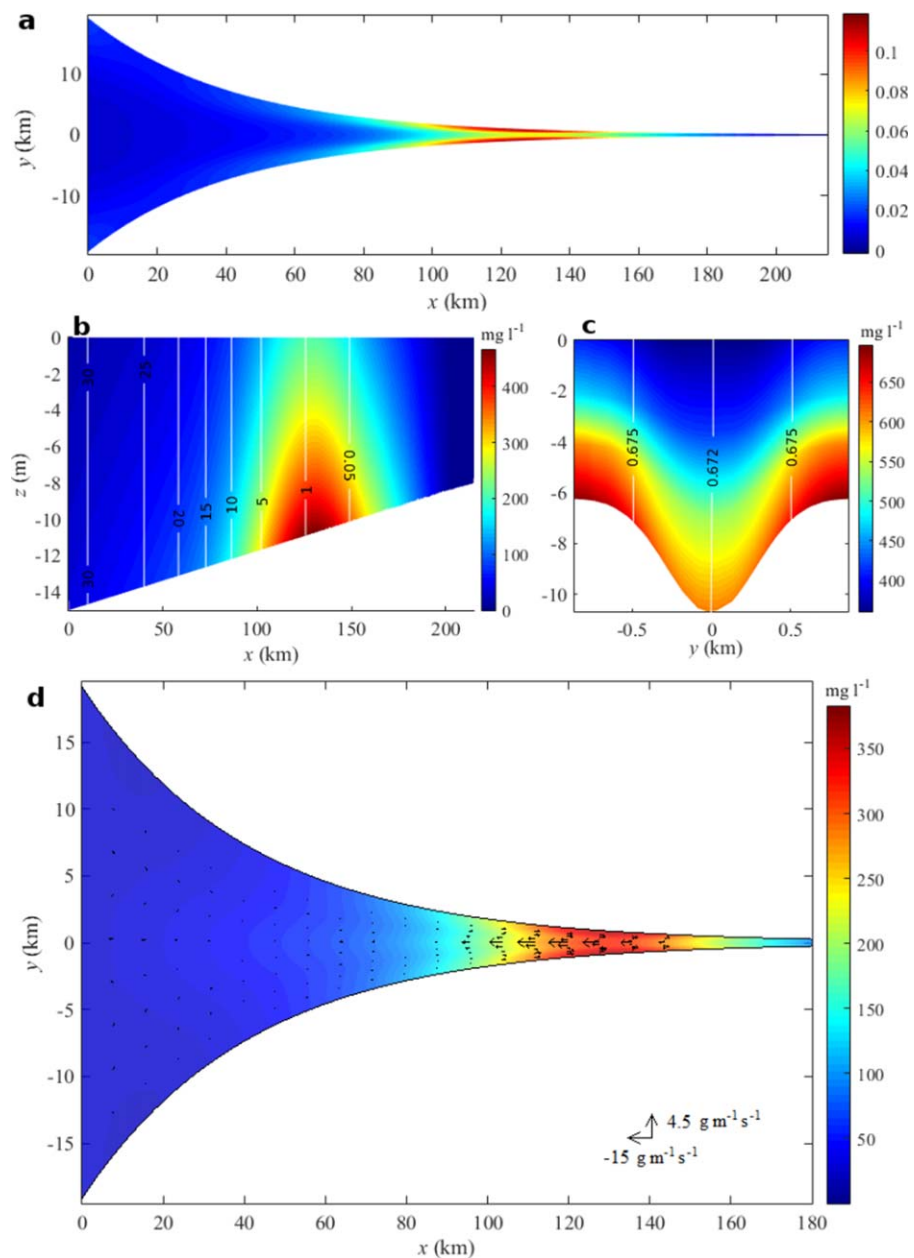


Figure 13. Same as Figure 8, but for $Q = 72 \text{ m}^3 \cdot \text{s}^{-1}$. The cross section in Figure 13c is taken at $x = 130 \text{ km}$.

sea (for less than 10 km), with most sediments trapped in a small region in the central estuary (see Figure 14b). Excluding the gravitational circulation hardly changes longitudinal location of the ETM, but the maximum sediment concentration is reduced (see Figure 14c).

5.2.2. High River Discharge

By increasing the river discharge from 288 to $864 \text{ m}^3 \cdot \text{s}^{-1}$, the maximum sediment availability is found near the mouth (Figure 15a). The salt intrusion is dramatically reduced, with the 1 psu isohaline at the central axis of the estuary shifting from $\sim 125 \text{ km}$ to $\sim 55 \text{ km}$ from the mouth (see white lines in Figure 15b). The maximum residual suspended sediment concentration at the central axis of the estuary is found at $x \sim 50 \text{ km}$ (Figure 15b), coinciding the 5 psu isohaline. The residual SSC at $x = 50 \text{ km}$ is larger in the deeper channel than on the shoals, and the sediment concentrations become more laterally uniform (Figure 15c). Within the ETM region ($x < 60 \text{ km}$), sediments are transported landward through the deeper channel, laterally transporting toward the flanks, and subsequently transported seaward over the shoals (see arrows in

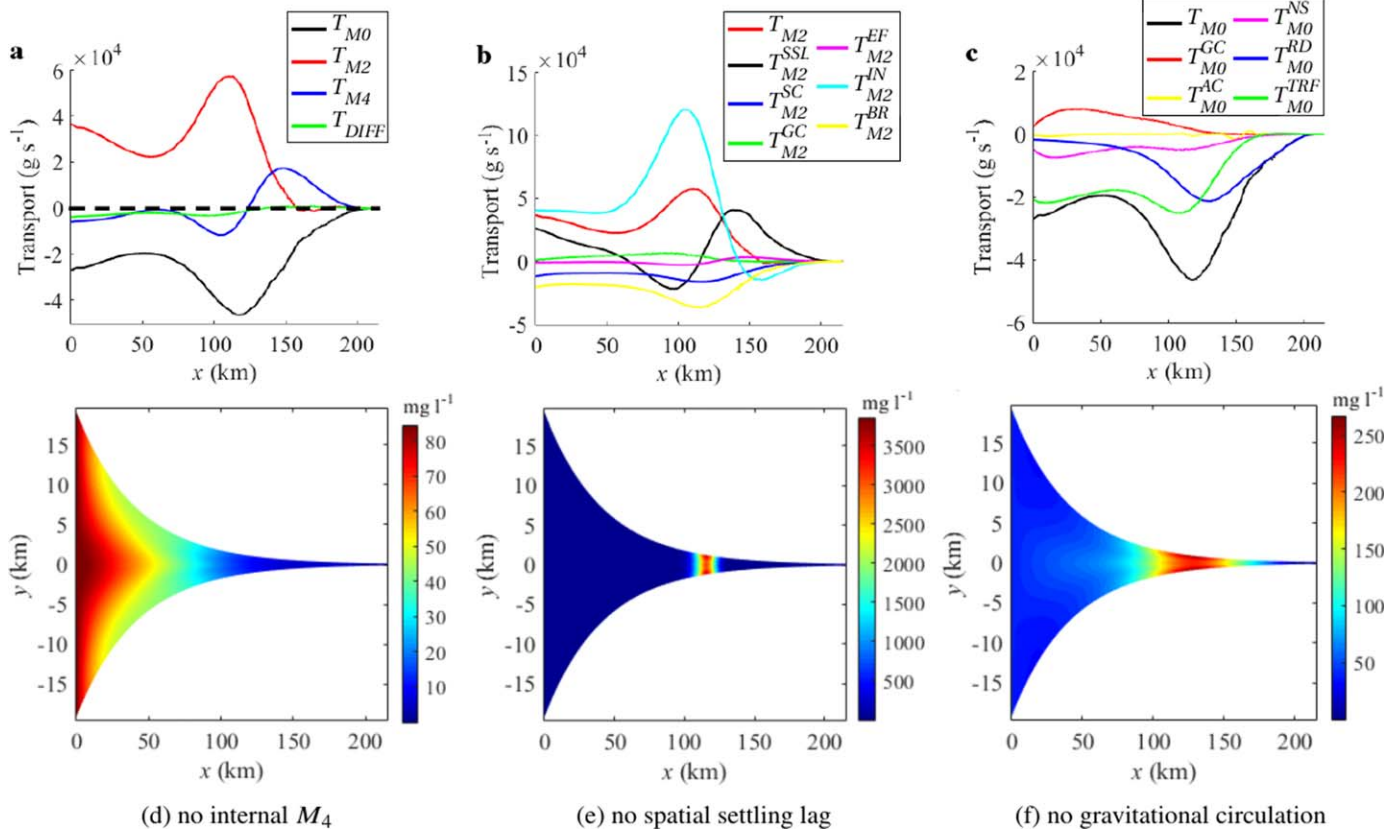


Figure 14. Same as (top) Figure 6 and (bottom) Figure 7, but for $Q = 72 \text{ m}^3 \cdot \text{s}^{-1}$.

Figure 15d). Moreover, it is found that the maximum depth-averaged residual concentrations are located in the center of the transport circulation cells.

For $Q = 864 \text{ m}^3 \cdot \text{s}^{-1}$, the sediment transport contributions T_{M_2} and T_{M_0} still dominate the cross-sectionally integrated residual sediment balance (Figure 16a). The major changes in this balance are that, the sediment transport contributions due to M_2 tidal advection of the M_2 tidal concentrations related to the internally generated M_4 overtide ($T_{M_2}^{IN}$) decreases and that related to the spatial settling lag effects ($T_{M_2}^{SSL}$) increases. The landward sediment transport contributions induced by gravitational circulation ($T_{M_2}^{GC}$ and $T_{M_0}^{GC}$) are also increased. As a result, excluding the sediment transport related to any of these three contributions results in an ETM at the mouth (see Figures 16d–16f).

The main changes of the relative importance of residual sediment transport contributions by varying river discharge are also summarized in Table 3. By decreasing (increasing) river discharge, the river-induced residual flow is decreased (increased), and the ebb-dominant bed shear stress becomes less (more) significant. This results in a reduced residual sediment transport contribution due to advection of residual SSC by river-induced flow ($T_{M_0}^{RD}$) and a reduced residual transport due to M_2 tidal advection of the M_2 tidal concentration as a result of the river-induced ebb-dominant bed shear stress (included in $T_{M_2}^{BR}$). Moreover, decreasing (increasing) river discharge results in smaller (larger) longitudinal and lateral salinity gradients, hence decreasing (increasing) the residual sediment transport contributions related to gravitational circulation ($T_{M_2}^{GC}$, $T_{M_0}^{GC}$), see Table 3. Decreasing (increasing) river discharge also results in narrower (wider) ETM region, which results in a more (less) important residual sediment transport contribution due to spatial settling lag effects ($T_{M_2}^{SSL}$). The residual sediment transport contributions due to other mechanisms ($T_{M_2}^{IN}$, $T_{M_0}^{TRF}$) become more (less) dominant, maintaining the balance of the residual sediment transport over the cross section for equilibrium.

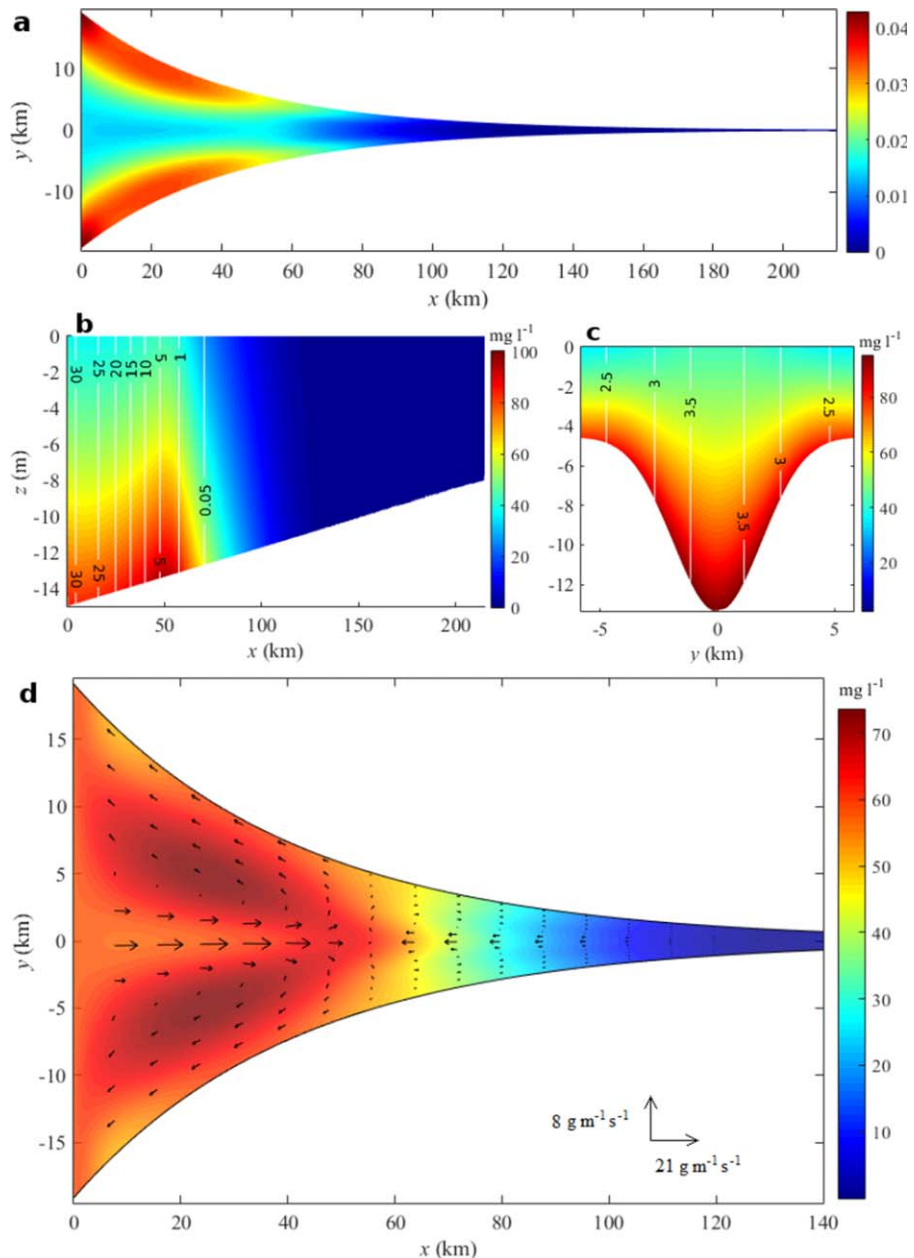


Figure 15. Same as Figure 8, but for $Q = 864 \text{ m}^3 \cdot \text{s}^{-1}$. The cross section in Figure 15c is taken at $x = 50 \text{ km}$.

6. Model Limitations

6.1. Deviations From Observations

This model requires the net sediment transport through both the seaward and landward boundaries to vanish, so that the total amount of sediment in the estuary remains unchanged and the condition of morphodynamic equilibrium is satisfied. In real estuaries, however, the net sediment transport from the mouth and the landward end may not cancel each other (depending on the strength of tide/wind forcing, river flow, and the sediment availabilities in the adjacent ocean and upper rivers). This would result in a nonequilibrium state with pointwise deposition/erosion in the estuary and a temporally varying sediment availability distribution. The sediment transport processes in these cases can thus differ significantly from those in equilibrium.

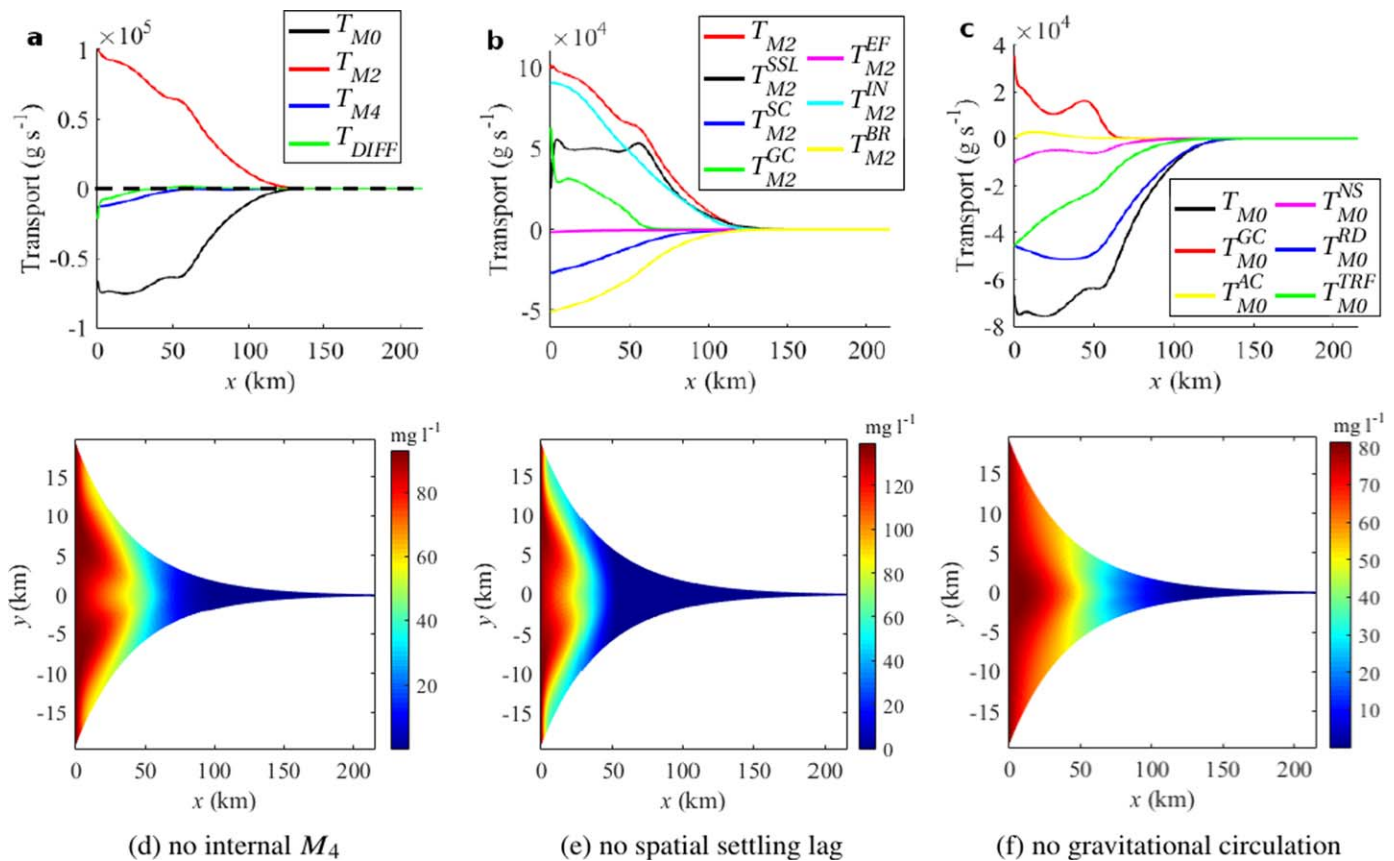


Figure 16. Same as (top) Figure 6 and (bottom) Figure 7, but for $Q = 864 \text{ m}^3 \cdot \text{s}^{-1}$.

A major difference between the model results and the observational results of McSweeney et al. (2016b) is that, in the observations, the cross-sectionally integrated tidally averaged sediment transport due to tidal pumping can vary from up-estuary to down-estuary with increasing river discharges, while in the present model tidal pumping always results in a landward sediment transport. This inconsistency can be understood by noting that the sediment transport in the model is obtained assuming the estuary to be in morphodynamic equilibrium, while the observed sediment transport is obtained under nonequilibrium conditions with time-varying forcing conditions such as river discharge and tides. This hypothesis is tested by recalculating the residual sediment transport contribution due to tidal pumping under a small river discharge condition, using the sediment availability which is obtained under a large river discharge condition. Test results show that the tidal pumping contribution results in a significant seaward residual sediment transport. This suggests that by increasing river discharge, the tidal pumping contribution tends to transport sediment seaward to reach a new morphodynamic equilibrium.

In fact, even though the model assumes morphodynamic equilibrium, it can be used to predict the changes of sediment transport contributions and ETM's during spring-neap variations and river fluctuations when sediment deposition and erosion can actually take place. For instance, since salinity and sediment availability usually lag behind spring-neap tidal variations, the salt and sediment transport patterns during the transition from neap to spring can be predicted by forcing the model with a strong (spring) tide but using S and a calculated with a weak (neap) tide. The resulting salt and sediment transport patterns can be thus tested against observations during early spring tides. Similarly, since the adjustment time of sediment availability after high-flow events (e.g., months) is usually much larger than that of river fluctuations (e.g., days), the variations of ETM's and sediment transport contributions during low river discharges can be predicted by forcing the model with a small Q while using a calculated with a large Q . For this case, the simulated ETM features and sediment transport patterns can be tested against field data during the early stage of the low-flow period.

6.2. Unresolved Processes

Even though many processes contributing to sediment transport and trapping are resolved in the model presented in this paper, there are a number of processes which are potentially important but not taken into account. Among these processes are the sediment transport related to the residual flow due to the covariance between the temporally varying eddy viscosity and shear (Burchard & Hetland, 2010; Burchard & Schuttelaars, 2012; Burchard et al., 2011; Dijkstra et al., 2017; Jay & Musiak, 1994), constrained sediment resuspension in case of strong salinity-induced stratifications in the lower water column (Geyer, 1993; Scully & Friedrichs, 2003, 2007) and sediment-induced residual currents (Talke et al., 2009). Beyond that, the effects of the critical bed shear stress and hindered settling are not considered. Last but not least, flocculation, which is evidenced to be important in the region of low salinities in the Delaware estuary (Gibbs et al., 1983), is also excluded in the model.

For example, in case of the Delaware estuary, the simulated ETM for a river discharge of $Q = 864 \text{ m}^3 \cdot \text{s}^{-1}$ is located at a much more seaward position compared to the observations of Sommerfield and Wong (2011). This deviation is related to the underestimated salt intrusion (Wei et al., 2017) and the landward sediment transport induced by gravitational circulation due to neglecting the stratification effects during high river flows. Limited by the well-mixed assumption, the top-to-bottom salinity difference obtained from this model is less than 1.5 psu for $Q = 864 \text{ m}^3 \cdot \text{s}^{-1}$ (Wei et al., 2017). However, according to the observations of McSweeney et al. (2016a), the top-to-bottom salinity difference in the channel of the Delaware Bay reaches up to 10 psu for $Q = 688 \text{ m}^3 \cdot \text{s}^{-1}$ (during neap tides). This strong stratification can significantly suppress vertical mixing, effectively increasing the tidal advective diffusivity (Wei et al., 2016) and estuarine circulations (Lerczak & Geyer, 2004), thus enhancing salt intrusion and gravitational circulation (Lerczak et al., 2009; Ralston et al., 2008; Wei et al., 2017). Stratification also strongly affects the cross-sectional distribution of SSC: stratification constrains sediment suspension to the lower water column (McSweeney et al., 2016b); meanwhile, sediments suspended from the deeper channel are constrained in the channel due to the significantly inhibited transverse circulation/transport (Lerczak & Geyer, 2004). This results in much higher SSC's near the bottom of the channel (than in the rest of the cross section), coinciding with the strongest landward currents induced by gravitational circulation (Wei et al., 2017). Therefore, including the stratification effects would result in a much more significant landward sediment transport due to gravitational circulation during neap tides and large river flows, and result in an ETM more upstream.

7. Conclusion

The sediment transport and trapping in estuaries are important to estuarine morphology, ecology and economy, but the dominant physical mechanisms behind the three-dimensional sediment dynamics are not well understood. This paper introduces a semi-analytical 3-D model to identify the dominant mechanisms governing the sediment transport and trapping in well-mixed estuaries. This model resolves the three-dimensional dynamic effects of salinity on water motion and sediment transport. As a study case, the sediment dynamics in a schematized estuary with a channel-shoal structure and an exponentially decreasing width is studied. This study case considers a river discharge of $288 \text{ m}^3 \cdot \text{s}^{-1}$ and a constant sediment settling velocity of $0.5 \text{ mm} \cdot \text{s}^{-1}$, which are representative for the Delaware estuary. As a first step, Coriolis is ignored. The maximum suspended sediment concentration (SSC) is found near the salt intrusion limit, with larger concentrations on the shoals than in the deeper channel. The depth-integrated residual sediment transport shows remarkable symmetric circulation cells: downstream of the ETM, sediments are transported from the seaward region to the ETM through the deeper channel and transported from the ETM toward the sea over the shoals. Within the ETM region, sediments are transported landward over the shoals and transported from the landward regions to the ETM through the deeper channel. The longitudinal component of these transports is dominated by the advection of (mainly M_2) tidal suspended sediment concentrations by tidal currents (also called as the tidal pumping contribution), and advection of residual concentrations by residual currents. The lateral transport component, however, is mainly controlled by advection of the residual concentrations by the gravitational circulation.

The cross-sectionally integrated residual seaward sediment transport is dominated by advection of the residual suspended sediment concentration by river-induced flow and tidal return flow. The landward

sediment transport is mainly controlled by advection of the M_2 tidal concentrations by M_2 tidal currents. This transport contribution is accomplished through many different mechanisms. Among these the most important ones are related to the internally generated M_4 tidal currents, spatial settling lag effects and gravitational circulation. First of all, the asymmetric bed shear stress due to interactions of the internally generated M_4 bottom current and the M_2 bottom current results in an M_2 tidal component of the suspended sediment concentration which temporally correlates with the M_2 tidal currents and results in a residual sediment transport. This is the most important mechanism contributing to the landward residual sediment transport. Moreover, the temporal correlation between M_2 tidal velocities and the residual and M_4 tidal components of concentrations also results in an M_2 tidal concentration, which interacts with the M_2 tidal currents and results in a significant landward sediment transport. Besides, the advection of the residual concentrations by gravitational circulation, and the M_2 tidal advection of the M_2 tidal concentration (which is originated from the asymmetric bed shear stress due to the combined M_2 tidal and salinity-induced residual bottom currents), also contribute significantly to the landward residual sediment transport. The former two sediment transport contributions related to the internally generated M_4 overtide and spatial settling lag effects are essential for the formation of the ETM in the central region of the estuary. The transport contributions due to gravitational circulation, however, mainly affects the lateral distribution of the suspended sediments.

Including Coriolis force results in an asymmetric SSC distribution with respect to the central axis of the estuary, with larger residual concentrations on the right shoal than on the left, looking seaward. The depth-integrated sediment transport shows one circulation cell with sediments transported landward from the left side of the estuary and seaward from the right. These results are qualitatively consistent with the observations of McSweeney et al. (2016b) for the river discharge considered here. The relative importance of different sediment contributions is hardly influenced by the Coriolis effects.

The characteristics of the ETM and the relative importance of different residual sediment transport contributions are significantly influenced by sediment settling velocity. By decreasing the settling velocity from 0.5 to $0.2 \text{ mm}\cdot\text{s}^{-1}$, the ETM moves downstream of the salt intrusion limit, with much larger residual suspended sediment concentrations on the shoals than in the deeper channel. Residual sediment transport is significant within the ETM region, where sediments are transported landward through the deeper channel and seaward over the shoals. The M_2 tidal advection of the M_2 tidal component of concentrations related to the internally generated M_4 tide and spatial settling lag effects dominates the cross-sectionally integrated landward residual sediment transport. The advection of the M_2 tidal concentrations (which is related to the gravitational circulation) by the M_2 tidal currents results in a seaward sediment transport integrating over the cross section. This mechanism contributes significantly to trapping sediments in the downstream region. By increasing the settling velocity to $1 \text{ mm}\cdot\text{s}^{-1}$, the ETM remains near the salt intrusion limit in the central region of the estuary, while the residual suspended sediment concentrations become larger in the deeper channel than on the shoals. Significant residual sediment transports are found within the ETM with sediments transported seaward through the deeper channel and landward over the shoals. The M_2 tidal advection of M_2 tidal concentrations related to the internally generated M_4 tide predominates the landward residual sediment transport integrated over the cross section, while that related to spatial settling lag effects controls the width of the ETM by transporting sediments from the ETM to regions further downstream or upstream. The suspended sediment transport related to the gravitational circulation makes a more significant contribution to the landward residual sediment transport.

The ETM moves slightly landward by decreasing the river discharge to $72 \text{ m}^3\cdot\text{s}^{-1}$. For this river discharge, the landward residual sediment transport is predominantly controlled by the M_2 tidal advection of the M_2 tidal concentrations related to the internally generated M_4 tide. The residual sediment transport due to the spatial settling lag effects contributes significantly in transporting sediments from the ETM region and controls the width of the ETM. By increasing the river discharge to $864 \text{ m}^3\cdot\text{s}^{-1}$, the ETM moves significantly toward the sea. The sediment transport contributions due to the M_2 tidal advection of the M_2 tidal concentrations related to the internally generated M_4 tide and spatial settling lag effects, and the advective transport related to the gravitational circulation, are all essential to the landward residual sediment transport and the formation of the ETM.

Acknowledgments

This work is funded by China scholarship Council (CSC, File 201206710049), and is part of the research programme NWO-ALW project 8843.10.005, financed by the Netherlands Organisation for Scientific Research(NWO) and the Chinese Organisation for Scientific Research (NSFC). The work is sponsored by NWO Exacte Wetenschappen (Physical Sciences) for using supercomputer facilities with financial support from the Nederlandse Organisatie voor Wetenschappelijk Onderzoek (Netherlands Organization for Scientific Research, NWO). We appreciate for the comments from two anonymous reviewers which have greatly helped to improve the clarity of the paper. The observational data referred to in this study are available from references; the model data can be downloaded from the zenodo website (<https://zenodo.org/record/846840#.WZxnbK2E37h>).

References

Aubrey, D. (1986). Hydrodynamic controls on sediment transport in well-mixed bays and Estuaries. In J. van de Kreeke (Ed.), *Physics of shallow estuaries and bays* (pp. 245–258). New York, NY: Springer-Verlag.

Becherer, J., Flöser, G., Umlauf, L., & Burchard, H. (2016). Estuarine circulation versus tidal pumping: Sediment transport in a well-mixed tidal inlet. *Journal of Geophysical Research: Oceans*, 121, 6251–6270. <https://doi.org/10.1002/2016JC011640>

Biggs, R., & Church, T. (1984). *The Delaware Estuary: Research as a background for estuarine management and development*. Newark, DE: Sea Grant College Program, University of Delaware.

Burchard, H., & Baumert, H. (1998). The formation of estuarine turbidity maxima due to density effects in the salt wedge. A hydrodynamic process study. *Journal of Physical Oceanography*, 28(2), 309–321.

Burchard, H., Bolding, K., & Villarreal, M. R. (2004). Three-dimensional modelling of estuarine turbidity maxima in a tidal estuary. *Ocean Dynamics*, 54(2), 250–265.

Burchard, H., & Hetland, R. D. (2010). Quantifying the contributions of tidal straining and gravitational circulation to residual circulation in periodically stratified tidal estuaries. *Journal of Physical Oceanography*, 40(6), 1243–1262.

Burchard, H., Hetland, R. D., Schulz, E., & Schuttelaars, H. M. (2011). Drivers of residual estuarine circulation in tidally energetic estuaries: Straight and irrotational channels with parabolic cross section. *Journal of Physical Oceanography*, 41(3), 548–570.

Burchard, H., & Schuttelaars, H. M. (2012). Analysis of tidal straining as driver for estuarine circulation in well-mixed estuaries. *Journal of Physical Oceanography*, 42(2), 261–271.

Chernetsky, A. S., Schuttelaars, H. M., & Talke, S. A. (2010). The effect of tidal asymmetry and temporal settling lag on sediment trapping in tidal estuaries. *Ocean Dynamics*, 60(5), 1219–1241.

de Jonge, V. N., Schuttelaars, H. M., van Beusekom, J. E., Talke, S. A., & de Swart, H. E. (2014). The influence of channel deepening on estuarine turbidity levels and dynamics, as exemplified by the ems estuary. *Estuarine, Coastal and Shelf Science*, 139, 46–59.

De Swart, H., & Zimmerman, J. (2009). Morphodynamics of tidal inlet systems. *Annual Review of Fluid Mechanics*, 41, 203–229.

Dijkstra, Y. M., Schuttelaars, H. M., & Burchard, H. (2017). Generation of exchange flows in estuaries by tidal and gravitational eddy viscosity–shear covariance (ESCO). *Journal of Geophysical Research: Oceans*, 122(5), 4217–4237.

Festa, J. F., & Hansen, D. V. (1978). Turbidity maxima in partially mixed estuaries: A two-dimensional numerical model. *Estuarine and Coastal Marine Science*, 7(4), 347–359.

Fredsoe, J., & Deigaard, R. (1992). *Mechanics of coastal sediment transport* (Vol. 3). Singapore: World Scientific.

Friedrichs, C., Armbrust, B., & Swart, H. D. (1998). Hydrodynamics and equilibrium sediment dynamics of shallow, funnel-shaped tidal estuaries. In J. Dronkers & M. B. A. M. Scheffers (Eds.), *Physics of estuaries and coastal seas* (pp. 315–327). Rotterdam, the Netherlands: Balkema.

Friedrichs, C. T., & Hamrick, J. M. (1996). Effects of channel geometry on cross sectional variations in along channel velocity in partially stratified estuaries. In D. G. Aubrey & C. T. Friedrichs (Eds.), *Buoyancy effects on coastal and estuarine dynamics* (pp. 283–300). Washington, DC: American Geophysical Union.

Fugate, D. C., Friedrichs, C. T., & Sanford, L. P. (2007). Lateral dynamics and associated transport of sediment in the upper reaches of a partially mixed estuary, Chesapeake Bay, USA. *Continental Shelf Research*, 27(5), 679–698.

Geyer, W. R. (1993). The importance of suppression of turbulence by stratification on the estuarine turbidity maximum. *Estuaries*, 16(1), 113–125.

Gibbs, R. J., Konwar, L., & Terchunian, A. (1983). Size of flocs suspended in Delaware Bay. *Canadian Journal of Fisheries and Aquatic Sciences*, 40(51), s102–s104.

Grabemann, I., Uncles, R., Krause, G., & Stephens, J. (1997). Behaviour of turbidity maxima in the Tamar (UK) and Weser (FRG) estuaries. *Estuarine, Coastal and Shelf Science*, 45(2), 235–246.

Huijts, K., Schuttelaars, H., De Swart, H., & Valle-Levinson, A. (2006). Lateral entrainment of sediment in tidal estuaries: An idealized model study. *Journal of Geophysical Research: Oceans*, 111, C12016. <https://doi.org/10.1029/2006JC003615>.

Huijts, K. M., de Swart, H. E., Schramkowski, G. P., & Schuttelaars, H. M. (2011). Transverse structure of tidal and residual flow and sediment concentration in estuaries. *Ocean Dynamics*, 61(8), 1067–1091.

Ianniello, J. P. (1977). Tidally induced residual currents in estuaries with constant breadth and depth. *Journal of Marine Research*, 35, 755–786.

Jay, D., Talke, S., Hudson, A., & Twardowski, M. (2015). Estuarine turbidity maxima revisited: Instrumental approaches, remote sensing, modeling studies, and new directions. In P. J. Ashworth, J. L. Best, & D. R. Parsons (Eds.), *Developments in sedimentology* (Vol. 68, 49–109). Amsterdam, the Netherlands: Elsevier.

Jay, D. A., & Musiak, J. D. (1994). Particle trapping in estuarine tidal flows. *Journal of Geophysical Research*, 99(C10), 20445–20461.

Kumar, M., Schuttelaars, H. M., & Roos, P. C. (2017). Three-dimensional semi-idealized model for estuarine turbidity maxima in tidally dominated estuaries. *Ocean Modelling*, 113, 1–21.

Kumar, M., Schuttelaars, H. M., Roos, P. C., & Möller, M. (2016). Three-dimensional semi-idealized model for tidal motion in tidal estuaries. *Ocean Dynamics*, 66(1), 99–118.

Lerczak, J. A., & Geyer, W. R. (2004). Modeling the lateral circulation in straight, stratified estuaries. *Journal of Physical Oceanography*, 34(6), 1410–1428.

Lerczak, J. A., Geyer, W. R., & Ralston, D. K. (2009). The temporal response of the length of a partially stratified estuary to changes in river flow and tidal amplitude. *Journal of Physical Oceanography*, 39(4), 915–933.

Lin, J., & Kuo, A. Y. (2001). Secondary turbidity maximum in a partially mixed microtidal estuary. *Estuaries*, 24(5), 707–720.

Lin, J., & Kuo, A. Y. (2003). A model study of turbidity maxima in the York River Estuary, Virginia. *Estuaries*, 26(5), 1269–1280.

McCarthy, R. K. (1993). Residual currents in tidally dominated, well-mixed estuaries. *Tellus, Series A: Dynamic Meteorology and Oceanography*, 45(4), 325–340.

McSweeney, J. M., Chant, R. J., & Sommerfield, C. K. (2016b). Lateral variability of sediment transport in the Delaware Estuary. *Journal of Geophysical Research: Oceans*, 121, 725–744. <https://doi.org/10.1002/2015JC010974>

McSweeney, J. M., Chant, R. J., Wilkin, J. L., & Sommerfield, C. K. (2016a). Suspended-sediment impacts on light-limited productivity in the Delaware Estuary. *Estuaries and Coasts*, 1–17.

Postma, H. (1967). Sediment transport and sedimentation in the estuarine environment. In G. H. Lauff (Ed.), *Estuaries* (pp. 158–179). Washington, DC: American Association for the Advancement of Science.

Ralston, D. K., Geyer, W. R., & Lerczak, J. A. (2008). Subtidal salinity and velocity in the Hudson River Estuary: Observations and modeling. *Journal of Physical Oceanography*, 38(4), 753–770.

- Ralston, D. K., Geyer, W. R., & Warner, J. C. (2012). Bathymetric controls on sediment transport in the Hudson River Estuary: Lateral asymmetry and frontal trapping. *Journal of Geophysical Research: Oceans*, *117*, C10013. <https://doi.org/10.1029/2012JC008124>
- Ralston, D. K., Warner, J. C., Geyer, W. R., & Wall, G. R. (2013). Sediment transport due to extreme events: The Hudson River Estuary after tropical storms Irene and Lee. *Geophysical Research Letters*, *40*, 5451–5455. <https://doi.org/10.1002/2013GL057906>
- Sanford, L. P., Suttles, S. E., & Halka, J. P. (2001). Reconsidering the physics of the Chesapeake Bay estuarine turbidity maximum. *Estuaries*, *24*(5), 655–669.
- Schoellhamer, D. H., Mumley, T. E., & Leatherbarrow, J. E. (2007). Suspended sediment and sediment-associated contaminants in san francisco bay. *Environmental Research*, *105*(1), 119–131.
- Schramkowski, G. P., & De Swart, H. (2002). Morphodynamic equilibrium in straight tidal channels: Combined effects of coriolis force and external overtides. *Journal of Geophysical Research: Oceans*, *107*(C12), 3227. <https://doi.org/10.1029/2000JC000693>
- Schuttelaars, H. M., de Jonge, V. N., & Chernetsky, A. (2013). Improving the predictive power when modelling physical effects of human interventions in estuarine systems. *Ocean & Coastal Management*, *79*, 70–82.
- Scully, M. E., & Friedrichs, C. T. (2003). The influence of asymmetries in overlying stratification on near-bed turbulence and sediment suspension in a partially mixed estuary. *Ocean Dynamics*, *53*(3), 208–219.
- Scully, M. E., & Friedrichs, C. T. (2007). Sediment pumping by tidal asymmetry in a partially mixed estuary. *Journal of Geophysical Research: Oceans*, *112*, C07028. <https://doi.org/10.1029/2006JC003784>
- Sommerfield, C. K., & Wong, K.-C. (2011). Mechanisms of sediment flux and turbidity maintenance in the Delaware Estuary. *Journal of Geophysical Research: Oceans*, *116*, C01005. <https://doi.org/10.1029/2010JC006462>
- Talke, S. A., de Swart, H. E., & Schuttelaars, H. (2009). Feedback between residual circulations and sediment distribution in highly turbid estuaries: An analytical model. *Continental Shelf Research*, *29*(1), 119–135.
- Uncles, R., & Stephens, J. (1993). Nature of the turbidity maximum in the Tamar Estuary, UK. *Estuarine, Coastal and Shelf Science*, *36*(5), 413–431.
- Van Maren, D., Van Kessel, T., Cronin, K., & Sittoni, L. (2015). The impact of channel deepening and dredging on estuarine sediment concentration. *Continental Shelf Research*, *95*, 1–14.
- Walters, R. A. (1997). A model study of tidal and residual flow in Delaware Bay and river. *Journal of Geophysical Research*, *102*(C6), 12689–12704.
- Wei, X., Kumar, M., & Schuttelaars, H. M. (2017). Three-dimensional salt dynamics in well-mixed estuaries: Influence of estuarine convergence, coriolis and bathymetry. *Journal of Physical Oceanography*, *47*(7).
- Wei, X., Schramkowski, G. P., & Schuttelaars, H. M. (2016). Salt dynamics in well-mixed estuaries: Importance of advection by tides. *Journal of Physical Oceanography*, *46*(5), 1457–1475.
- Winant, C. D. (2008). Three-dimensional residual tidal circulation in an elongated, rotating basin. *Journal of Physical Oceanography*, *38*(6), 1278–1295.
- Winterwerp, J. C. (2011). Fine sediment transport by tidal asymmetry in the high-concentrated ems river: Indications for a regime shift in response to channel deepening. *Ocean Dynamics*, *61*(2–3), 203–215.
- Winterwerp, J. C., & Wang, Z. B. (2013). Man-induced regime shifts in small estuaries—I: Theory. *Ocean Dynamics*, *63*(11–12), 1279–1292.
- Yang, Z., de Swart, H. E., Cheng, H., Jiang, C., & Valle-Levinson, A. (2014). Modelling lateral entrapment of suspended sediment in estuaries: The role of spatial lags in settling and m 4 tidal flow. *Continental Shelf Research*, *85*, 126–142.